The Astronomical Journal, 158:138 (21pp), 2019 October https://doi.org/10.3847/1538-3881/ab3467

The Revised *TESS* Input Catalog and Candidate Target List

Keivan G. Stassun[1,2], Ryan J. Oelkers[1], Martin Paegert[3], Guillermo Torres[3], Joshua Pepper[4], Nathan De Lee[5], Kevin Collins[1], David W. Latham[3], Philip S. Muirhead[6], Jay Chittidi[7,8], Bárbara Rojas-Ayala[9], Scott W. Fleming[10], Mark E. Rose[11], Peter Tenenbaum[11], Eric B. Ting[11], Stephen R. Kane[12], Thomas Barclay[13,14], Jacob L. Bean[15], C. E. Brassuer[10], David Charbonneau[3], Jian Ge[16], Jack J. Lissauer[11], Andrew W. Mann[17], Brian McLean[10], Susan Mullally[10], Norio Narita[18,19,20,21], Peter Plavchan[22], George R. Ricker[23], Dimitar Sasselov[3], S. Seager[23,24,25,26], Sanjib Sharma[27], Bernie Shiao[10], Alessandro Sozzetti[28], Dennis Stello[27,29,30], Roland Vanderspek[23], Geoff Wallace[10], and Joshua N. Winn[31]

[1] Vanderbilt University, Department of Physics & Astronomy, 6301 Stevenson Center Lane, Nashville, TN 37235, USA
[2] Fisk University, Department of Physics, 1000 18th Avenue N., Nashville, TN 37208, USA
[3] Center for Astrophysics, Harvard & Smithsonian, 60 Garden Street, Cambridge, MA 02138, USA
[4] Lehigh University, Department of Physics, 16 Memorial Drive East, Bethlehem, PA, 18015, USA
[5] 1 Department of Physics, Geology, and Engineering Technology, Northern Kentucky University, Highland Heights, KY 41099, USA
[6] Department of Astronomy, Institute for Astrophysical Research, Boston University, 725 Commonwealth Avenue, Boston, MA 02215, USA
[7] Department of Physics & Astronomy, Vassar College, Poughkeepsie, NY 12604, USA
[8] Maria Mitchell Observatory, 4 Vestal Street, Nantucket, MA 02554, USA
[9] Departamento de Ciencias Fisicas, Universidad Andres Bello, Fernandez Concha 700, Las Condes, Santiago, Chile
[10] Space Telescope Science Institute, 3700 San Martin Drive, Baltimore, MD 21218, USA
[11] NASA Ames Research Center, Moffett Field, CA 94035, USA
[12] Department of Earth and Planetary Sciences, University of California, Riverside, CA 92521, USA
[13] NASA Goddard Space Flight Center, 8800 Greenbelt Road, Greenbelt, MD 20771, USA
[14] University of Maryland, Baltimore County, 1000 Hilltop Circle, Baltimore, MD 21250, USA
[15] Department of Astronomy & Astrophysics, University of Chicago, Chicago, IL 60637, USA
[16] 211 Bryant Space Science Center, Department of Astronomy, University of Florida, Gainesville, FL 32611, USA
[17] Department of Physics and Astronomy, University of North Carolina at Chapel Hill, Chapel Hill, NC 27599, USA
[18] Astrobiology Center, 2-21-1 Osawa, Mitaka, Tokyo 181-8588, Japan
[19] JST, PRESTO, 2-21-1 Osawa, Mitaka, Tokyo 181-8588, Japan
[20] National Astronomical Observatory of Japan, 2-21-1 Osawa, Mitaka, Tokyo 181-8588, Japan
[21] Instituto de Astrofísica de Canarias (IAC), E-38205 La Laguna, Tenerife, Spain
[22] Department of Physics & Astronomy, MS 3F3, George Mason University, 4400 University Drive, Fairfax, VA 22030, USA
[23] Kavli Institute for Astrophysics and Space Research, Massachusetts Institute of Technology, Cambridge, MA 02139, USA
[24] Department of Physics, Massachusetts Institute of Technology, Cambridge, MA 02139, USA
[25] Department of Earth, Atmospheric and Planetary Sciences, Massachusetts Institute of Technology, Cambridge, MA 02139, USA
[26] Department of Aeronautics and Astronautics, MIT, 77 Massachusetts Avenue, Cambridge, MA 02139, USA
[27] Sydney Institute for Astronomy (SIfA), School of Physics, University of Sydney, NSW 2006, Australia
[28] INAF—Osservatorio Astrofisico di Torino, Via Osservatorio 20, I-10025 Pino Torinese, Italy
[29] School of Physics, University of New South Wales, NSW 2052, Australia
[30] Stellar Astrophysics Centre, Department of Physics & Astronomy, Aarhus University, Ny Munkegade 120, DK-8000 Aarhus C, Denmark
[31] Department of Astrophysical Sciences, Princeton University, Princeton, NJ 08544, USA

Received 2019 May 25; revised 2019 July 20; accepted 2019 July 22; published 2019 September 9

Abstract

We describe the catalogs assembled and the algorithms used to populate the revised *TESS* Input Catalog (TIC), based on the incorporation of the *Gaia* second data release. We also describe a revised ranking system for prioritizing stars for 2 minute cadence observations, and we assemble a revised Candidate Target List (CTL) using that ranking. The TIC is available on the Mikulski Archive for Space Telescopes server, and an enhanced CTL is available through the Filtergraph data visualization portal system at http://filtergraph.vanderbilt.edu/tess_ctl.

Key words: stars: fundamental parameters

1. Introduction

The *Transiting Exoplanet Survey Satellite* (*TESS*) Input Catalog (TIC) is a comprehensive collection of sources on the sky, for use by the *TESS* mission to select target stars to observe and to provide stellar parameters useful for the evaluation of transit signals. The TIC is intended to enable the selection of optimal targets for the planet transit search, to enable calculation of flux contamination in the *TESS* aperture for each target, and to provide reliable stellar radii for calculating planetary radii, which in turn determines the targets that will receive mission-supported photometric and spectroscopic follow-up. The TIC is also essential for the community to select targets through the Guest Investigator program.

The area of the sky projected onto each *TESS* pixel is large ($21 \times 21''$) and the point-spread function (PSF) is typically 1–2 pixels in radius (depending on stellar brightness and position in the focal plane). Consequently, the photometric aperture surrounding a given *TESS* target may include flux from multiple objects. Therefore, it is important that the TIC contain every optically luminous, persistent, nonmoving object in the sky, down to the limits of available wide-field photometric point-source catalogs.

An initial version of the TIC for use in the first year of *TESS* observations was delivered shortly before *TESS* launch in early 2018 and is described in detail by Stassun et al. (2018). It had been intended from the start of planning for the *TESS* mission (Ricker et al. 2015) that the ~1 billion point sources with parallaxes and proper motions expected from the *Gaia* mission (Gaia Collaboration et al. 2018) would provide an ideal basis for the TIC. Unfortunately, the final data release schedule for *Gaia* only allowed the first data release (DR1) to be available prior to *TESS* launch; thus, the initial version of the TIC included parallaxes for only the ∼2 million bright stars in the *Tycho-Gaia* Astrometric Solution (TGAS; Gaia Collaboration et al. 2016). By necessity, then, the majority of the ∼470 million stars in the TIC had their properties calculated from broadband photometry (and spectroscopy in a tiny minority of cases) on the basis of a complex set of logic rules, algorithms, and empirical relations (see also Brown et al. 2011; Huber et al. 2016; Berger et al. 2018; Deacon et al. 2019) customized for the *TESS* bandpass (Stassun et al. 2018).

Importantly, as a result of the small number of stars with measured parallaxes, it was not possible to calculate radii accurately for the vast majority of the stars in the TIC. Therefore, it was necessary to use a proper-motion-based criterion to screen out evolved stars for the Candidate Target List (CTL), from which the ∼200,000 targets for the 2 minute cadence transit search are selected, according to the *TESS* mission requirements (see Section 3). Because the proper-motion-based method is not able to distinguish subgiants from dwarfs, the CTL inevitably included a large number of subgiants; we estimated that as many as ∼50% of the stars in the CTL were subgiants (see Stassun et al. 2018 for a detailed discussion). Finally, in order to ensure inclusion of known high-value targets, the TIC and CTL were manually populated by a set of specially curated lists, including a Bright Star list, a Cool Dwarf list, a list of Known Planet Hosts, and a list of Hot Subdwarfs (see Appendix A for a detailed discussion).

Shortly after the *TESS* launch, *Gaia* delivered its second data release (DR2; Gaia Collaboration et al. 2018), which includes parallaxes as well as estimated stellar properties for 1.3 billion stars. In addition to enabling a more direct determination of the stellar radii, and therefore a more optimized selection of transit targets for the CTL, the availability of uniform photometry via the three *Gaia* bandpasses (G, $G_{\rm BP}$, $G_{\rm RP}$) greatly simplifies the process of calculating various stellar properties via a smaller, consolidated set of algorithms and empirical relations.

The purpose of this paper is to describe the updated TIC and CTL. Section 2 describes the construction of the TIC and the algorithms used to calculate various stellar quantities. Section 3 describes the construction of the CTL, the additional algorithms used for parameters unique to the CTL, and in particular the prioritization scheme for selecting targets for 2 minute cadence observations. Finally, Section 4 provides a summary of the contents of the TIC and CTL.

The TIC and CTL are also accompanied by official release notes, which are provided on the Mikulski Archive for Space Telescopes (MAST) server. Public access to the TIC is also provided via the MAST server, and access to an enhanced CTL is provided via the Filtergraph data visualization service at https://filtergraph.vanderbilt.edu/tess_ctl.

2. The TIC

In this section, we detail the algorithms, relations, and rules adopted for populating the TIC. The TIC includes a number of columns, each with a specified format and a permitted range of values. These are summarized by Stassun et al. (2018). The provenance flags associated with various TIC quantities are listed in Appendix B. It is important to understand that, as described below, the TIC deliberately includes both point sources (stars) and extended sources (e.g., galaxies); positional searches of the TIC will in general return some extended sources as well as stars. For a more detailed discussion about extended sources in the TIC, see Stassun et al. (2018). These can be separated by use of the `objtype` flag (see Appendix B). Finally, a number of specially curated lists are summarized in Appendix A.

2.1. Assembly of the TIC

For the TIC that was produced for the first year of the *TESS* mission (Stassun et al. 2018), we adopted the Two Micron All Sky Survey (2MASS) catalog as the base point-source catalog, and we referenced all other data to the 2MASS point source. As shown in Figure 1, reproduced from Stassun et al. (2018) for convenience, this included a large number of catalogs containing spectroscopic quantities, photometry in the various passbands that we utilized to estimate various stellar properties, proper motions, and a number of other ancillary data. Because the *Gaia* DR2 catalog was not yet available at the time of *TESS* launch, the TIC that was delivered at that time only included the *Gaia* DR1 parallaxes, again cross-referenced to the 2MASS base catalog. Now we have rebuilt the TIC with *Gaia* DR2 as the base. An updated visual overview, analogous to Figure 1, is shown in Figure 2 and described in detail in the following subsections.

2.2. Point Sources

The base point-source catalog for the TIC is *Gaia* DR2. In order to preserve continuity and provenance with the previous version of the TIC, which was based on the 2MASS catalog, we first translated all previous TIC sources to the new TIC catalog using the association between *Gaia* and 2MASS that is provided within *Gaia* DR2 itself.

TIC coordinates and their uncertainties have been propagated to epoch 2000 because of mission requirements. The error propagation leads to much larger uncertainties than those native to the nominal *Gaia* DR2 positions. Especially for *Gaia* DR2 stars, users should not try to propagate forward the TIC coordinates using the proper motions listed. Instead, users should use the original *Gaia* DR2 positions, proper motions, and corresponding errors for propagation. We provide the original R.A. and decl. with errors as given in the source catalog (*Gaia* DR2, 2MASS, and so on) in additional columns on MAST and Filtergraph.

Due to the improved angular resolution and depth of the *Gaia* DR2 catalog relative to 2MASS, there were a large number of cases where a single 2MASS source turned out to be associated with two *Gaia* sources. In these cases, we retain the association of the one 2MASS identifier with both *Gaia* sources, but we set the JHK_S magnitudes of both sources to null because there was no definitive means for splitting the reported 2MASS flux among the two *Gaia* sources. While we have not done so here for the sake of catalog purity, we note that in principle it is possible to estimate the 2MASS JHK_S magnitudes for the two sources from the *Gaia*-reported $GG_{\rm BP}G_{\rm RP}$ fluxes and the relations provided by Evans et al. (2018). For the purposes of the TIC, we require only the *Gaia*-reported $GG_{\rm BP}G_{\rm RP}$ magnitudes, as described below, to which we applied the corrections for bright stars ($G < 6$) as reported by Evans et al. (2018). There were also ∼33 million cases of

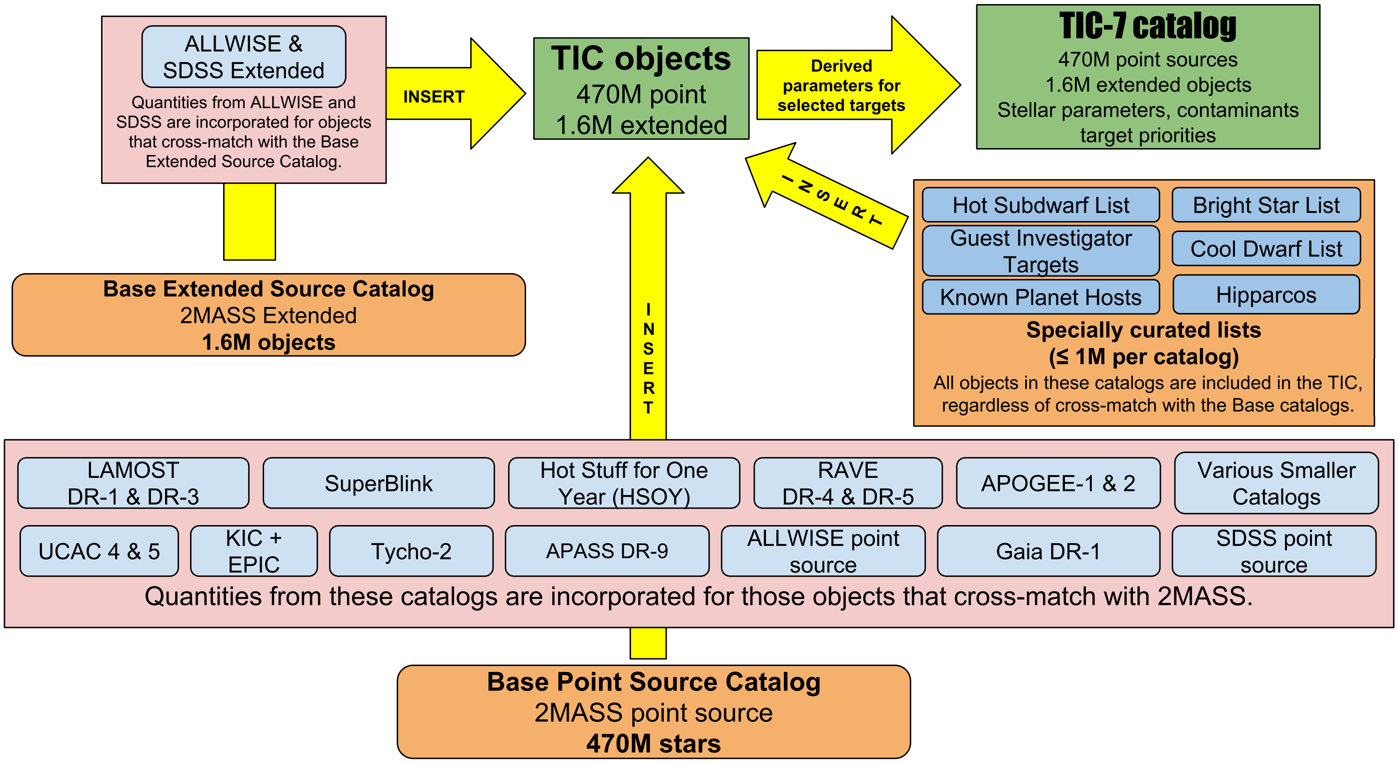

Figure 1. Visual representation of the assembly of TICv7 as produced for the first year of the *TESS* mission (reproduced from Figure 1 of Stassun et al. 2018).

2MASS sources that had no *Gaia* counterpart. We expect that many of these stars are 2MASS artifacts around bright stars, but we did not identify a straightforward way to identify them consistently and therefore have left them unaltered for TICv8.

While we calculate the stellar properties for most TIC stars from *Gaia* magnitudes via the relations discussed below, where possible we adopt measured spectroscopic parameters. Following the conventions of the initial TIC, we selected effective temperatures ($T_{\rm eff}$) and metallicities ([Fe/H]) when available, from the following catalogs and in the order of preference shown in Table 1. Users are cautioned that surface gravities ($\log g$) are always *calculated* in TICv8 using the TICv8-reported mass and radius; $\log g$ is not adopted from spectroscopic catalogs even when available so as to ensure internal consistency of $\log g$ with mass and radius. Note also that while metallicities are reported when available from spectroscopic catalogs, this is for convenience only, and we do not use metallicity in any relations or derived quantities.

2.3. Algorithms for Calculated Stellar Parameters

In this section, we describe the algorithmic procedures we adopted to calculate various stellar parameters. We begin with the procedure for calculating an apparent magnitude in the *TESS* bandpass, T, as this is the most basic quantity required of any object in the TIC. Since many of the subsequent empirical relations that we adopt depend on the effective temperature ($T_{\rm eff}$), we next describe the procedures for determining $T_{\rm eff}$. Briefly, we prefer spectroscopic $T_{\rm eff}$ if available and if the reported error[32] is less than 300 K; otherwise we calculate $T_{\rm eff}$ from photometric colors via empirical relations that we describe. These photometric colors must first be corrected for reddening, so we first also describe our photometric dereddening procedures.

We next apply cuts based on the *Gaia* DR2 quality flags on astrometry[33] and photometry (see Arenou et al. 2018, Equations (1) and (2)), such that objects failing these quality criteria do not have any other stellar parameters computed. In these cases, if stellar parameters had been computed for the CTL in TICv7, then we adopt those parameters again here.

Note that wherever our relations involve the *Gaia* DR2 parallax, we utilize the Bayesian distance estimate from Bailer-Jones et al. (2018). This both provides a proper posterior estimate of the (generally asymmetric) errors in the distance and ensures that the distance estimate is nonnegative, because in some cases the native *Gaia* DR2 parallax can be negative. Finally, we defer a detailed discussion of the procedure for calculating parameter uncertainties to Section 3.2, where we describe a Monte Carlo based approach that we apply to objects in the CTL. Here we simply note that, for the TIC, which requires symmetric error bars to be reported, we take the arithmetic mean of the asymmetric error bars determined for CTL objects. In some cases, the resulting symmetrized error can be larger than the quantity itself; these cases should be regarded with caution.

[32] Note that, in order to ensure simple and systematically applicable criteria for adoption, we do not attempt to take quality flags from the input spectral catalogs into account; users are encouraged to check the flag values in the source catalogs where available.

[33] The *Gaia* astrometric quality parameter (u) has recently been improved by renormalization (see Lindegren 2018). This became public after the initial TICv8 was built (ESA published the most recently computed RUWE values for *Gaia* DR2 on 2019 June 10 at http://cdn.gea.esac.esa.int/Gaia/gdr2/ruwe/csv/), so we have not incorporated the "Renormalized Unit Weight Error" (RUWE) into the TICv8 quality assessment scheme. This could affect the choice of which stars we compute properties for in a small number of cases, but it does not affect the computed properties themselves.

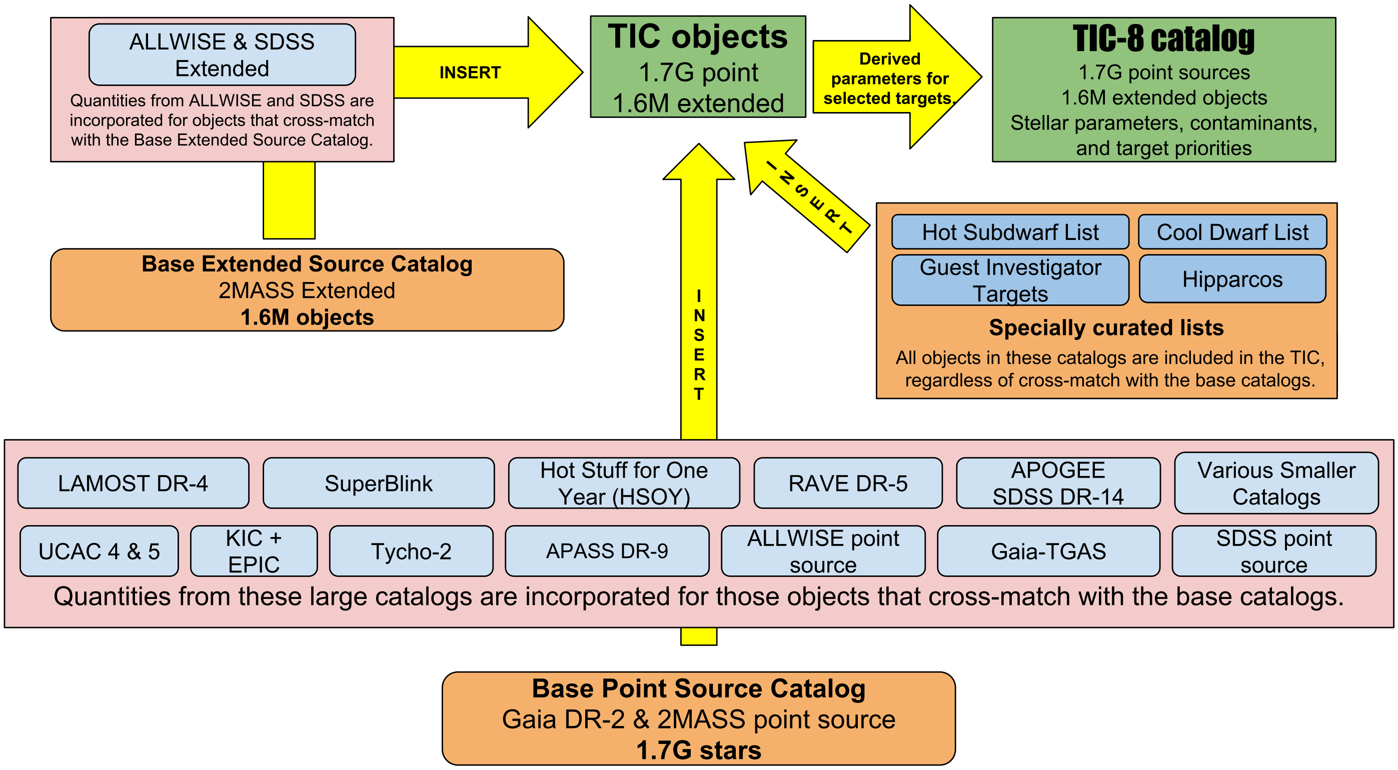

Figure 2. Visual representation of the assembly of TICv8.

Finally, where it is necessary to identify a star's evolutionary phase, for the purposes of this paper we adopt the same definitions as in Stassun et al. (2018):

1. Dwarfs: $\log g \geqslant 4.1$
2. Subgiants: $3.5 \leqslant \log g < 4.1$ (or $T_{\rm eff} \geqslant 5000$ K and $3.0 \leqslant \log g < 3.5$)
3. Giants: $\log g \leqslant 3.0$ (or $T_{\rm eff} < 5000$ K and $3.0 \leqslant \log g < 3.5$).

2.3.1. TESS *Magnitude*

The most basic quantity required for every TIC object, aside from its position, is its apparent magnitude in the *TESS* bandpass, which we represent as T. As we did in TICv7, we derived a relation based on the PHOENIX model atmospheres (Husser et al. 2016). We adopted the most up-to-date *TESS* passband available (R. Vanderspek 2019, private communication) and the *Gaia* passbands for G, $G_{\rm BP}$, and $G_{\rm RP}$ from Gaia Collaboration et al. (2018). Note that we did not apply the small corrections to the *Gaia* bandpasses from Maíz Apellániz & Weiler (2018) as these were not available prior to our construction of the base TIC.

The relation that we adopt,

$$T = G - 0.00522555(G_{\rm BP} - G_{\rm RP})^3 + 0.0891337(G_{\rm BP} - G_{\rm RP})^2 - 0.633923(G_{\rm BP} - G_{\rm RP}) + 0.0324473, \quad (1)$$

is valid for dwarfs, subgiants, and giants of any metallicity, and the formal scatter is 0.006 mag. The fit and residuals of the relation are shown in Figure 3. Strictly speaking, this relation is valid for $-0.2 < G_{\rm BP} - G_{\rm RP} < 3.5$, but we extrapolate it to $-1.0 < G_{\rm BP} - G_{\rm RP} < 6.0$ because by NASA requirement every star in the TIC must have a T magnitude. Even though the relation degrades considerably for M dwarfs ($G_{\rm BP} - G_{\rm RP} > 2$), we consider it to be the best available estimator from the G band. Most importantly, the refined T magnitudes provided in the specially curated Cool Dwarf list override the magnitudes computed by the relation above.

Of course, the use of stellar atmosphere models introduces some systematic error, so the true errors in the predicted T are likely to be larger than 0.006 mag. To estimate this, we used the same atmosphere models to derive a relation between V magnitude and the magnitudes in the *Gaia* passbands, and we compared our relation with the empirical relation reported by Evans et al. (2018). Their empirical relation is based on real V magnitudes for stars from various catalogs and from the measured G magnitudes for the same stars from *Gaia* DR2. Figure 4 compares the two relations. The comparison here is based on the set of stars from TICv7 that had spectroscopic $T_{\rm eff}$, so they are not the same set of stars used by Evans et al. (2018); however, this should not affect our conclusions significantly. A slight difference is evident between our model fit and the Evans et al. (2018) empirical fit, which is to be expected. However, the largest difference between the two relations is only $\sim$0.1 mag, providing confidence in our adopted relation and suggesting that the true uncertainties in our derived T are likely to be at most $\sim$0.1 mag in most cases.

The *TESS* magnitude relation above is strictly valid for unreddened stars. Because the measured magnitudes and colors from *Gaia* are typically affected by extinction, we first deredden the colors and correct the G magnitudes for extinction, then apply the relation to obtain a dereddened T magnitude, and finally add extinction back into T to obtain an apparent magnitude. The extinction coefficients required in each band are provided below in Section 2.3.3.

Table 1
Spectroscopic Catalogs in the TIC

Name	Data Release	Approximate No. of Stars	Priority	References
SPOCS	⋯	1.6 k	1	Brewer et al. (2016)
PASTEL	⋯	93 k	2	Soubiran et al. (2016)
Gaia-ESO	DR3	29 k	3	Gilmore et al. (2012)
TESS-HERMES	DR1	25 k	4	Sharma et al. (2018)
GALAH	DR2	340 k	5	Buder et al. (2018)
APOGEE-2	DR14	277 k	6	Abolfathi et al. (2018)
LAMOST	DR4	2.9 M	7	Luo et al. (2015)
RAVE	DR5	484 k	8	Kunder et al. (2017)
Geneva-Copenhagen	DR3	16 k	9	Holmberg et al. (2009)

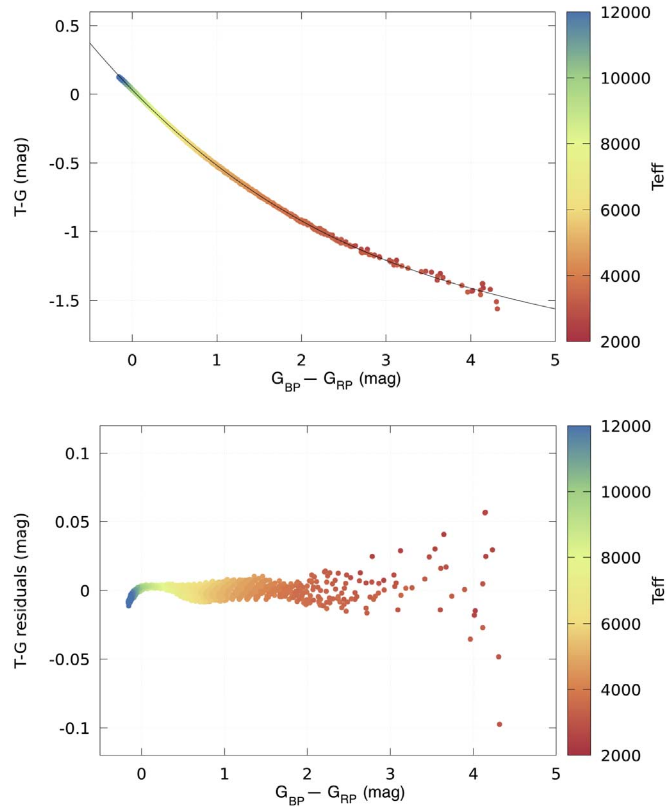

Figure 3. Derivation of our *TESS* magnitude relation. A polynomial fit to synthetic colors from PHOENIX models is shown at the top (equation given in the text), and residuals at the bottom.

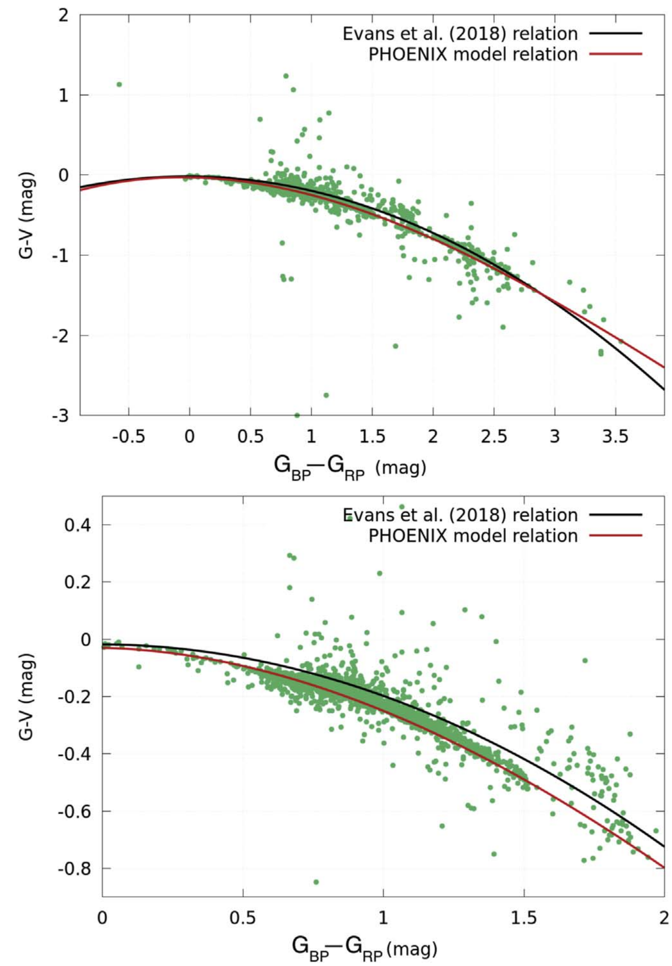

Figure 4. The top panel presents a comparison of our synthetic $G - V$ colors as a function of $G_{\rm BP} - G_{\rm RP}$ (polynomial red line fit) with a similar relation by Evans et al. (2018) shown in black. The bottom panel shows a close-up of the solar-color region. The points represent actual measurements for a set of stars from TICv7.

Finally, we have developed simple relations for stars that either have colors beyond the formal validity limits of the above relation or that do not have fluxes reported for all three *Gaia* passbands. For stars that are bluer or redder than the limits of the above relation, we simply extrapolate the same polynomial, but to be conservative we increase the formal errors by 0.1 mag (added in quadrature). For stars with no valid $G_{\rm BP} - G_{\rm RP}$ colors, but which have a valid G magnitude, we use the following simple offset:

$$T = G - 0.430. \quad (2)$$

This offset is the value that specifically corresponds to a star like the Sun, with a color of $G_{\rm BP} - G_{\rm RP} = 0.82$ based on the PHOENIX stellar atmosphere models. As a very conservative error, we assign 0.6 mag, which should be valid for all but the reddest M dwarfs, which are in any case dealt with via the specially curated Cool Dwarf list.

2.3.2. V *Magnitude*

For completeness and for maximum usability, we compute the apparent V magnitude for TIC stars that do not possess a measured V from TICv7 but which possess *Gaia* photometry, as follows, using the relations provided by the *Gaia* team (Evans et al. 2018):

$$V = G + 0.01760 + 0.006860(G_{\rm BP} - G_{\rm RP}) + 0.1732(G_{\rm BP} - G_{\rm RP})^2, \quad (3)$$

which has a reported scatter of about 0.046 mag.

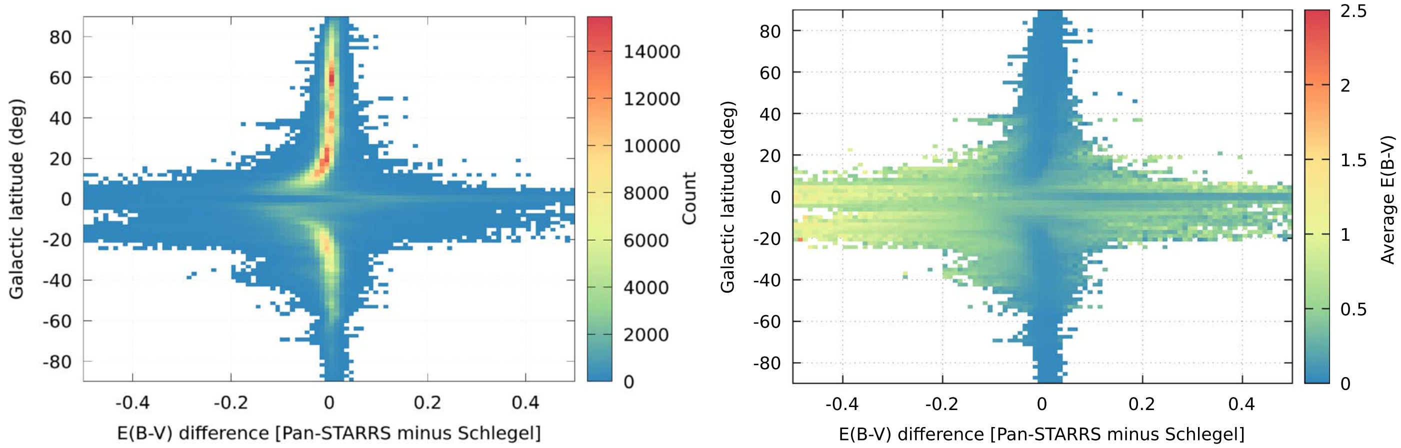

Figure 5. Left: comparison between the $E(B-V)$ reddening values returned by the Pan-STARRS and Schlegel extinction maps, as a function of Galactic latitude. Right: same, but color coded by average of $E(B-V)$.

2.3.3. Extinction and Dereddening

Because we estimate stellar $T_{\rm eff}$ principally from an empirical color relation involving the *Gaia* $G_{\rm BP}-G_{\rm RP}$ color (see Section 2.3.4), which is susceptible to reddening effects, it is necessary to first apply a dereddening correction, as we now describe.

When creating TICv7, we were limited by the available dust maps to estimates of the reddening along the full line of sight through the Galaxy in any particular direction, and we also were unable to estimate reddening within about 15 degrees of the Galactic plane. Here, we adopt the newly released three-dimensional, empirical, nearly all-sky dust maps from Pan-STARRS (Green et al. 2018), which provides an ability to estimate the reddening on a star-by-star basis according to the star's position in three dimensions (coordinates on the plane of the sky together with the distance). For the region of the sky not covered by Pan-STARRS (decl. below $-30°$), we continue to use the Schlegel et al. (1998) map, now with an adjustment to the total line-of-sight extinction for distance (from *Gaia*), assuming a standard exponential model for the disk with a scale height of 125 pc (see, e.g., Bonifacio et al. 2000). In both cases, we apply a recalibration coefficient of 0.884 to the $E(B-V)$ values, as prescribed by Schlafly & Finkbeiner (2011).

As an initial sanity check on the Pan-STARRS reddening estimates, we compared the $E(B-V)$ reddening values reported by the Pan-STARRS map against that estimated from the dust maps that we used in TICv7 (Schlegel et al. 1998). As shown in Figure 5, the agreement is in general quite good, with the $E(B-V)$ agreeing to within $\sim$0.05 mag for Galactic latitudes $|b|>15$ deg.

We require a relation to convert the $E(B-V)$ values that are provided by the reddening maps into $E(G_{\rm BP}-G_{\rm RP})$ and A_G for dereddening the *Gaia* $G_{\rm BP}-G_{\rm RP}$ and G observed colors. As the most common type of star in the TIC is similar to the Sun, we used a synthetic solar-like spectrum as the source ($T_{\rm eff}=5800$ K, $\log g=4.5$, $[{\rm Fe/H}]=0.0$, the closest PHOENIX model spectrum to the Sun) to compute the effective wavelengths for the various passbands following Equation (18) of Casagrande & VandenBerg (2014). We then used these mean wavelengths with the Cardelli et al. (1989) extinction law, which yields $E(G_{\rm BP}-G_{\rm RP})=1.31E(B-V)$ and $A_G=2.72E(B-V)$. We also used this procedure to determine the relation of $E(B-V)$ to A_T, the extinction in the *TESS* bandpass, for use in calculating the T magnitudes (see Section 2.3.1), which gives $A(T)=2.06E(B-V)$.

Applying the estimated reddening to the determination of $T_{\rm eff}$ via the photometric colors has the effect generally of making apparently cool stars hotter, and that hotter $T_{\rm eff}$ in turn has the effect of implying a larger radius and mass from our empirical relations described in Section 2.3.5. Therefore it is important to assess the quality of the dereddened $T_{\rm eff}$. Figure 6 (top) shows a comparison of the $T_{\rm eff}$ obtained from dereddened colors versus $T_{\rm eff}$ measured spectroscopically for $\sim$2 million stars from TICv7 with the relevant quantities available. As with all of the spectroscopic $T_{\rm eff}$ values that we adopt in the TIC, we limited the sample to stars whose spectroscopic $T_{\rm eff}$ values have reported uncertainties less than 300 K to ensure that the spectroscopic $T_{\rm eff}$ does not dominate the comparison of errors. The comparison overall is quite good, with a mean difference of 20 K and a 95th percentile range of -410 to $+220$ K. The slight skew toward negative $T_{\rm eff}$ differences (i.e., dereddened photometric $T_{\rm eff}$ being slightly cooler than the spectroscopic $T_{\rm eff}$) suggests that in some cases the reddening is underestimated (not enough dereddening correction applied), but this is at the margins of the overall distribution. Interestingly, as shown in Figure 6 (bottom), both the Pan-STARRS and Schlegel et al. (1998) dust maps appear to slightly overestimate the extinction toward the southern Galactic pole, resulting in our inferring a marginally elevated $T_{\rm eff}$ at $b\lesssim-70°$. Note that both G and T are broad photometric bands, which can complicate extinction corrections. In particular, the ratio of total to selective extinction, $R_G\equiv A_G/E(B-V)$, is a function of $T_{\rm eff}$ as well as the overall extinction A_V. The variation with A_V is small ($dR_G/dA_V\approx-0.03$) and can be ignored, but the variation with $T_{\rm eff}$ is slightly larger. This could also be a reason for the systematic trends seen in Figure 6 (top); see Figure A of Sanders & Das (2018) for further details and for one way to account for this.

Also shown in Figure 7 are the $T_{\rm eff}$ differences as a function of Galactic coordinates, where the effect of larger errors within $\sim$10 degrees of the plane is clear. Note that the Schlegel et al. (1998) dust maps have been shown to overestimate extinction for $E(B-V)>0.15$ by a factor of about 1.4 (Arce & Goodman 1999; Cambrésy et al. 2005); a correction is given in

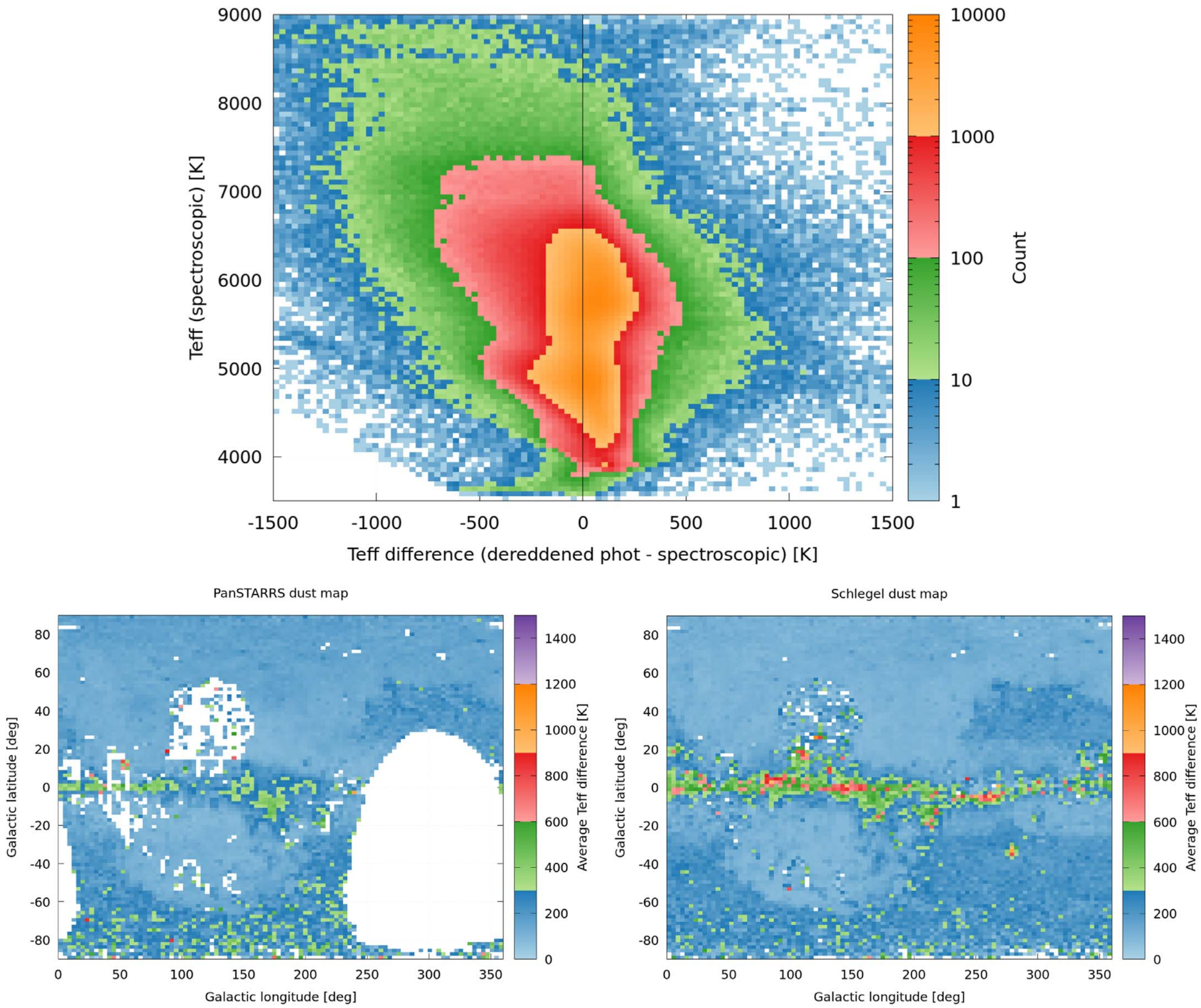

Figure 6. Comparison of T_{eff} from dereddened photometric colors versus spectroscopic. The median T_{eff} difference is ≈20 K, and the 95th percentile range is −410 to +220 K.

Equation (24) of Sharma et al. (2014). In any event, we reduce the CTL priority by a factor of 0.1 for stars within 10 degrees of the Galactic plane (see Section 3.3).

Finally, based on the comparisons above between the Pan-STARRS and Schlegel et al. (1998) dust maps, we find that only 1% of the ∼4 million stars compared have applied $E(B-V)$ values that disagree by more than 2.5 mag. This means that a star that in reality has a very low reddening could appear with $E(B-V)>2.5$ if the dust map at that location is such an extreme outlier. Thus, we adopt 2.5 as the maximum permissible $E(B-V)$ from the Schlegel et al. (1998) dust map (effectively a cap on A_V of ≈7.8) in cases where a reliable Pan-STARRS value is not available. In cases where there is not a reliable Pan-STARRS value and our adopted value from Schlegel et al. (1998) has been capped, we report the values, but do not apply any reddening in calculating the T magnitude, and we also do not attempt to provide any derived stellar parameters.

2.3.4. Effective Temperature

We derived a new empirical relation between T_{eff} and the *Gaia* $G_{\mathrm{BP}}-G_{\mathrm{RP}}$ colors, based on a set of 19,962 stars having spectroscopically determined T_{eff} and being within 100 pc so as to avoid reddening. We have ignored possible binarity, which is generally unknown for these reference stars and for stars in the larger TIC. After removing obvious outliers, we fit a spline function by eye. Figure 8 shows the fit, with the spline nodes marked with circles. Table 2 lists the nodes as ($G_{\mathrm{BP}}-G_{\mathrm{RP}}$, T_{eff}) pairs.

The residuals of the fit (see Figure 6, top panel) show a near-zero mean offset, with an rms scatter of 122 K. This seems quite reasonable: given the ∼100 K uncertainties typical of the spectroscopic T_{eff}, this would imply a true scatter in the photometric relation of ∼70 K. The range of validity of the relation is seen in the figure and is $G_{\mathrm{BP}}-G_{\mathrm{RP}}=[-0.2, +3.5]$, although the predictions are likely to be less reliable for hot stars with $G_{\mathrm{BP}}-G_{\mathrm{RP}}<0$ because of the very steep slope

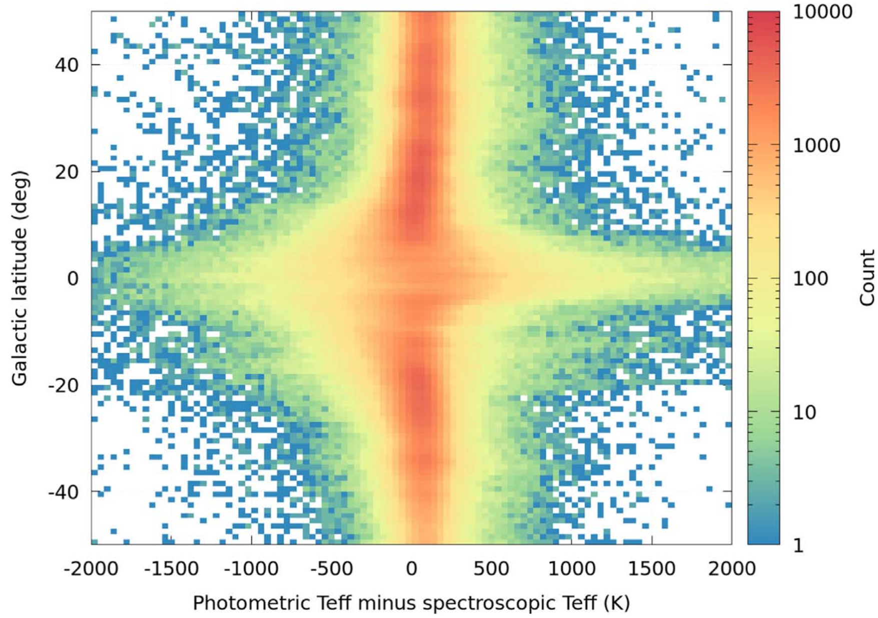

Figure 7. Comparison between photometric temperatures (based on *Gaia* colors dereddened using the Pan-STARRS dust map) and spectroscopic temperatures for the same stars, as a function of Galactic latitude.

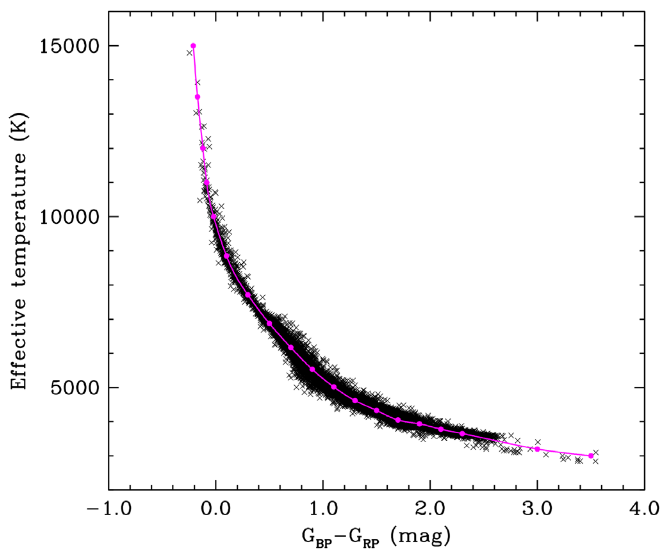

Figure 8. $T_{\rm eff}$ as a function of the $G_{\rm BP} - G_{\rm RP}$ color. See Table 2 for the nodes of the cubic spline fit.

Table 2
Spline Nodes for Relation in Figure 8

$G_{\rm BP}$–$G_{\rm RP}$	$T_{\rm eff}$
−0.21	15,000
−0.17	13,500
−0.12	12,000
−0.085	11,000
−0.02	10,000
0.1	8849.803711
0.3	7709.192383
0.5	6875.640137
0.7	6172.216309
0.9	5532.801758
1.1	5017.910156
1.3	4618.64209
1.5	4327.293457
1.7	4048.811523
1.9	3935.294434
2.1	3780.993652
2.3	3652.275635
3.00	3200
3.50	3000

of the relation, and also for M stars with $G_{\rm BP} - G_{\rm RP} > 2$. As discussed below, the CTL relies mainly on the specially curated Cool Dwarf list for cool dwarf stars and draws $T_{\rm eff}$ estimates for those stars from that list.

We note that metallicity has been ignored in deriving the above relation, largely because it is unknown for any given field star. The relation may therefore return somewhat biased values for stars with compositions very different for solar. For example, referring back to the top panel of Figure 6, we see the average shift between the photometric and spectroscopic temperatures is about +160 K if we restrict the comparison to stars more metal-poor than [Fe/H] = −1, and −80 K for stars more metal-rich than [Fe/H] = +0.35.

This relation provides a continuous color–$T_{\rm eff}$ relation from 3000 to 15,000 K. For stars with $G_{\rm BP} - G_{\rm RP}$ outside of this range of validity, the TIC reports $T_{\rm eff}$ = `Null`, unless a spectroscopic $T_{\rm eff}$ is available or if a $T_{\rm eff}$ is available from the CTL associated with TICv7. The final $T_{\rm eff}$ errors reported in the TIC from the above polynomial relation include the 122 K scatter added in quadrature to the uncertainties from the photometric errors.

2.3.5. Stellar Mass and Radius

We compute the stellar radii using the *Gaia* parallaxes, which we now have for every star in the CTL, according to the standard expression from the Stefan–Boltzmann relation:

$$\log(R/R_\odot) = \frac{1}{5}[4.74 - 5 + 5\log D - G - 10\log(T_{\rm eff}/5772) - {\rm BC}_G] \quad (4)$$

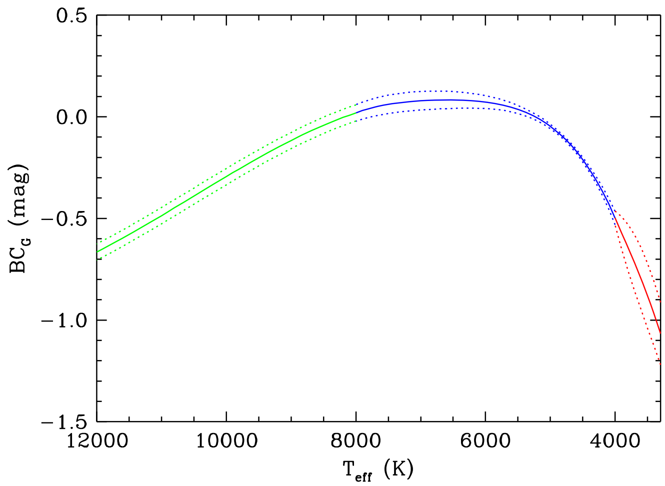

Figure 9. Bolometric corrections in the *Gaia* bandpass adopted in this work. Colors represent the three $T_{\rm eff}$ ranges for which we have adopted our BC_G versus $T_{\rm eff}$ relations, and dotted curves represent the adopted 1σ uncertainties for those relations.

where D is the distance based on the *Gaia* parallax from Bailer-Jones et al. (2018), G is the observed *Gaia* magnitude corrected for extinction ($G_{\rm obs} - A_G$), $T_{\rm eff}$ is the temperature from either spectroscopy or from dereddened colors, and BC_G is the bolometric correction in the *Gaia* passband as a function of $T_{\rm eff}$ (corrected for reddening if from colors). The above relation assumes that the object is a single star, and it will in general return biased values for the radius if it is a binary because the *Gaia* photometry will be affected by the companion. To be conservative, for $T_{\rm eff}$ from spectroscopy, we add 100 K in quadrature to the $T_{\rm eff}$ uncertainty if the catalog-reported $T_{\rm eff}$ uncertainty is less than 100 K when computing the resulting mass and radius uncertainties.

In order to develop a relation for BC_G as a function of $T_{\rm eff}$ for the widest possible $T_{\rm eff}$ range, we have adopted the following prescription (see Figure 9):

1. For the range 3300–8000 K, we adopt the polynomial formulae for BC_G reported by the *Gaia* team (Andrae et al. 2018, see their Equation (7) with coefficients in their Table 4), which are based on MARCS stellar atmosphere models within 0.5 dex of solar metallicity. Those relations come in two parts: 3300–4000 K[34] and 4000–8000 K. We have added a minor correction to the cooler segment—a shift of +0.0036 mag in the a_0 coefficient—in order to achieve continuity between the two segments. Andrae et al. (2018) also provide additional polynomials to describe the error in BC_G as a function of $T_{\rm eff}$, based essentially on the scatter as a function of $\log g$; we adopt these errors as well.
2. Above 8000 K, and up to the 12,000 K limit available in the PHOENIX library of stellar atmosphere models, we fit a cubic polynomial to the bolometric corrections from the models, restricted to metallicities within 0.5 dex of solar, as above. We chose to consider only $\log g$ values above 3.0, as our bolometric corrections here are intended for deriving radii of stars in the CTL only, from which we intentionally exclude giants. We shifted this polynomial by +0.01036 mag to match up exactly with the one from *Gaia* at 8000 K. For this hotter segment, we have adopted a constant error in BC_G of 0.04 mag based on the scatter as a function of $\log g$, which also provides continuity with the *Gaia* uncertainties.

The complete set of relations described above is therefore as follows:

For the range 3300–4000 K, and where $X \equiv T_{\rm eff} - 5772$ K,

$$BC_G = 1.7454 + 1.977 \times 10^{-3}X + 3.737 \times 10^{-7}X^2 - 8.966 \times 10^{-11}X^3 - 4.183 \times 10^{-14}X^4 \text{ mag.} \quad (5)$$

The uncertainty in BC_G is given by

$$\sigma_{BC_G} = -2.487 - 1.876 \times 10^{-3}X + 2.128 \times 10^{-7}X^2 + 3.807 \times 10^{-10}X^3 + 6.570 \times 10^{-14}X^4 \text{ mag.} \quad (6)$$

For the range 4000–8000 K,

$$BC_G = 0.0600 + 6.731 \times 10^{-5}X - 6.647 \times 10^{-8}X^2 + 2.859 \times 10^{-11}X^3 - 7.197 \times 10^{-15}X^4 \text{ mag} \quad (7)$$

with an uncertainty given by

$$\sigma_{BC_G} = 2.634 \times 10^{-2} + 2.438 \times 10^{-5}X - 1.129 \times 10^{-9}X^2 - 6.722 \times 10^{-12}X^3 + 1.635 \times 10^{-15}X^4 \text{ mag.} \quad (8)$$

For the range 8000–12,000 K,

$$BC_G = -3.70485 + 1.32935Y - 0.144609Y^2 + 0.00457793Y^3 \text{ mag} \quad (9)$$

where $Y \equiv T_{\rm eff}/1000$, with a constant uncertainty in BC_G of 0.04 mag. Note that the independent variable is different here, for numerical reasons.

This last polynomial should not be extrapolated beyond 12,000 K, so we are not able to compute BC_G (and therefore radius using the parallax) for $T_{\rm eff} > 12{,}000$ K. For stars cooler than 3300 K, the *Gaia* polynomial relation could in principle be extrapolated by a small amount, although in practice we adopt the stellar parameters for M dwarfs from the specially curated Cool Dwarf list.

We can infer stellar mass from $T_{\rm eff}$ for stars that are on the main sequence or not too far evolved from it. Therefore, we only apply our $T_{\rm eff}$–mass relation if the stellar radius places the star below the red giant branch and above the white dwarf sequence, as defined in Section 3.1 (see Figure 11). Note that we implicitly are reporting a mass for stars that are subgiants; these should be regarded with caution. However, the luminosities that are reported for these subgiants are expected to be reliable, as the luminosities depend only on radius and $T_{\rm eff}$ (see Section 2.4).

We have revised slightly the spline relations that we developed for stellar mass as a function of $T_{\rm eff}$ by Stassun et al. (2018), with the result that the formal errors are now somewhat smaller. Table 3 gives the spline nodes for the mean relation (unchanged from TICv7; Stassun et al. 2018) and the new nodal points for the lower and upper error bars, as

[34] There appears to be a discrepancy between the polynomial relation for the cooler segment by Andrae et al. (2018) and what is shown in their Figure 9. In that figure, the BC_G values extend a bit more negative at the cool end (to about −1.7) than indicated by their polynomial. We have not attempted to reconcile this discrepancy, but simply note it here for completeness.

Table 3
Updated Spline Relation for TICv8

Approx. Spectral Type	T_{eff}	Mean Mass	Lower Limit	Upper Limit
⋯	55,000	91.052	81.0	100.5
O5	42,000	40.0	36.0	44.0
B0	30,000	15.0	13.5	17.0
⋯	22,000	7.5	6.7	8.5
B5	15,200	4.4	3.95	4.95
B8	11,400	3.0	2.65	3.4
A0	9790	2.5	2.2	2.85
A5	8180	2.0	1.75	2.35
F0	7300	1.65	1.45	2.00
F5	6650	1.4	1.23	1.70
G0	5940	1.085	0.965	1.22
G5	5560	0.98	0.87	1.11
K0	5150	0.87	0.78	0.98
K5	4410	0.69	0.615	0.77
M0	3840	0.59	0.51	0.662
M2	3520	0.47	0.395	0.535
M5	3170	0.26	0.21	0.30
⋯	2800	0.117	0.091	0.14
⋯	2500	0.056	0.042	0.07

functions of T_{eff}. Approximate spectral types are also provided for convenience.

As an independent check on our derived stellar radii, we have compared our radii determined as above with those determined from fitting to stellar spectral energy distribution (SED) models by Deacon et al. (2019) and asteroseismically by Huber et al. (2017) for stars in common in the *Kepler* field. For Huber et al. (2017), we find very good agreement, as shown in Figure 10, with a mean difference of 0.64% and rms scatter of 7.03%, though with a slight skew toward larger radii in the TIC.

Comparing to Deacon et al. (2019) finds very good agreement as well. For ~843,000 stars in common, the mean radius from CTLv8 is 3.3% larger, which is about a 0.6σ offset. We observed a small number of large outliers due mainly to differences in the adopted distances; while TICv8 uses the Bayesian distance estimator from Bailer-Jones et al. (2018), Deacon et al. (2019) use the *Gaia* parallax directly, which can differ significantly for very small parallaxes.

2.4. Ensuring Internal Consistency in Derived Quantities

As described in the preceding sections, the basic stellar parameters that we determine for as many stars as possible are T_{eff} and radius, and we also then determine mass from T_{eff} where possible. To ensure that other reported stellar properties that are physically defined based on T_{eff}, radius, or mass, we always calculate those dependent quantities even when empirical measures are available from other catalogs. In particular, $\log g$ and mean density are always calculated from the mass and radius that we have determined. Similarly, we always calculate L_{bol} from the T_{eff} and radius that we have determined.

3. The CTL

The purpose of the CTL is to provide a subset of TIC objects that can be used to select the target stars for *TESS* 2 minute cadence observations in service of the *TESS* mission's primary science requirements, which are as follows:

1. Search >200,000 stars for planets with orbital periods less than 10 days and radii smaller than 2.5 $R_{\oplus}$.
2. Search for transiting planets with radii smaller than 2.5 $R_{\oplus}$ and with orbital periods up to 120 days among 10,000 stars in the ecliptic pole regions.
3. Determine masses for at least 50 planets with radii smaller than 4 $R_{\oplus}$.

Given the limited number of stars for which *TESS* will be able to acquire 2 minute cadence light curves, it is crucial that the set of targets for *TESS* be optimized for detection of small planets. To that end, we have compiled a catalog of bright stars that are likely to be dwarfs across the sky, from which a final target list for *TESS* can be drawn, based on in-flight observation constraints. This list of high-priority candidate 2 minute cadence targets is the CTL. Our basic consideration is to assemble a list of dwarf stars all over the sky in the temperature range of interest to *TESS*, bright enough for *TESS* to observe, and taking extra steps to include the scientifically valuable M dwarfs.

Our overall approach is to start with the ~1.7 billion stars in the TIC, and then apply cuts to select stars of the desired ranges in apparent magnitude and spectral type and to eliminate evolved stars. At this stage, we also compute additional information that is relevant for target selection, which, for logistical reasons or computational limitations, we do not compute for all other stars in the TIC.

First, we give a brief overview describing the assembly of the CTL from the TIC, including specifically the process by which we identify likely dwarf stars for inclusion in the CTL and identify likely red giants and white dwarfs for exclusion from the CTL. Next we describe the algorithms by which we calculate improved measures of uncertainties on the stellar parameters and flux contamination in the expected photometric aperture of each star (Section 3.2). Finally, we present the prioritization scheme used to identify the top-priority targets from the CTL for targeting (Section 3.3). The CTL is provided for use through MAST and for interactive use via the Filtergraph data visualization system (Burger et al. 2013) at http://filtergraph.vanderbilt.edu/tess_ctl. A summary of the quantities included in the CTL on the Filtergraph portal is provided in Appendix C.

3.1. Selection of Target Stars for the CTL

From the ~1.7 billion point sources in the TIC, we initially select stars for the CTL if they (1) have parallaxes and $GG_{RP}G_{BP}$ photometry reported by *Gaia* DR2 that satisfy quality criteria on reduced χ^2, number of degrees of freedom, photometric excess factor, and the G and $G_{BP} - G_{RP}$ colors (see Equations (1) and (2) in Arenou et al. 2018); and (2) satisfy the condition $T < 13$. We implement the T criterion to reduce the CTL to a manageable size, emphasizing the bright dwarfs that are likely to be the highest priority targets. Note that while this T cut would by itself eliminate many M dwarfs, we rely on the specially curated Cool Dwarf list to ensure the inclusion of high-priority, bona fide M dwarfs.

Next, we cut on stellar radius to eliminate red giants, as shown in Figure 11. Note that this explicitly includes subgiants ($3.5 < \log g < 4.1$); recognizing that some subgiants can be considered high value in some cases, we include them but rely on

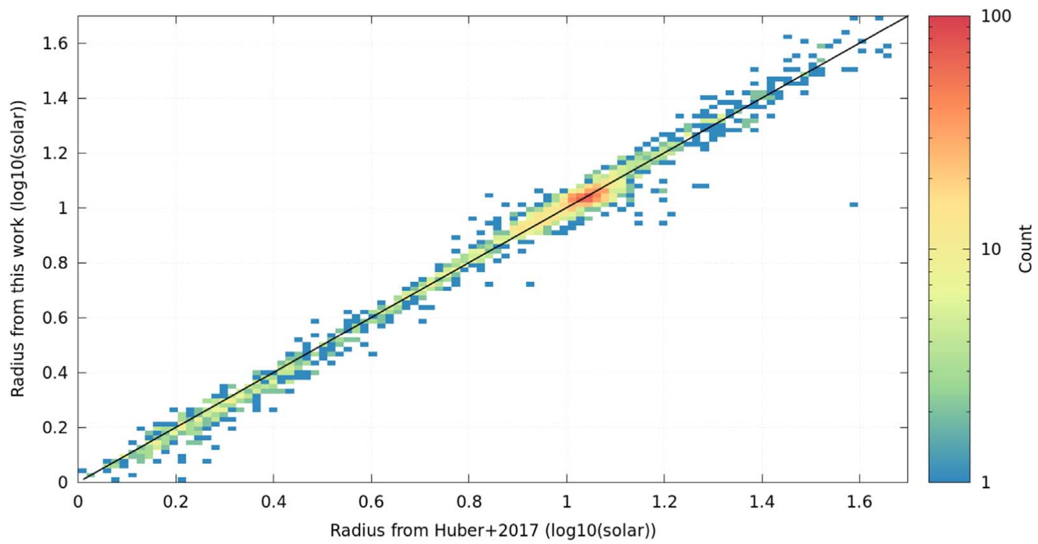

Figure 10. Comparison of stellar radii determined in the TIC versus those determined asteroseismically by Huber et al. (2017) for stars in the *Kepler* field.

the target prioritization metric and its dependence on stellar radius (see below) to ensure that bright subgiants do not overwhelm the selection of final 2 minute cadence targets. The specific radius cuts adopted as a function of $T_{\rm eff}$ are as follows (see Figure 11): for $T_{\rm eff} \geqslant 6000$ K, the dividing line is $\log R/R_{\odot} = 0.7$; then the nodes for the subsequent piecewise linear dividing lines are ($T_{\rm eff}$, $\log R/R_{\odot}$) = (5000 K, 0.2) and (2000 K, 0.0).

To exclude stars likely to be white dwarfs, we used a diagram of absolute G magnitude versus $G_{\rm BP} - G_{\rm RP}$ color (Figure 11, bottom panel), which shows the main sequence and white dwarf sequences clearly separated. We defined a boundary by eye, represented by the equation $M_G = 5.15$ $(G_{\rm BP} - G_{\rm RP}) + 4.12$ and shown by the line in Figure 11. We eliminated stars below this boundary (after proper corrections for reddening) as being probable white dwarfs.

The entire procedure described above is summarized in logical flowchart form in Figure 12. We do not include stars in the CTL if we are unable to determine their $T_{\rm eff}$ spectroscopically or from dereddened colors (see Section 2.3.3), or if we are unable to estimate their radius (Section 2.3.5) or the flux contamination from nearby stars (Section 3.2.1) since these are essential to setting target priorities (see Section 3.3). All stars in the specially curated Cool Dwarf and Hot Subdwarf target lists (Appendix A) are included in the CTL. Finally, in order to ensure inclusion of high-priority stars that may be missing from *Gaia* DR2, stars previously included in the CTL of TICv7 on the basis of a reduced proper-motion cut suggesting that they are dwarfs, and for which *Gaia* DR2 does not provide sufficiently reliable information to warrant their exclusion (according to the quality criteria discussed above), are included in the CTL. The CTL at present comprises 9.48 million stars.

Strictly speaking, the CTL as delivered to NASA is simply a list of candidate target stars with associated relative targeting priorities. We are providing an enhanced version of the CTL, with all relevant observed and derived stellar quantities described here, through the Filtergraph Portal system as a tool for the community to interact with this unique data set. Appendix C describes each quantity in the CTL that can be found on the Filtergraph Portal system.

3.2. Algorithms for Calculated Stellar Parameters

3.2.1. Flux Contamination

We follow the same procedures as in the original CTL (Stassun et al. 2018), with the same assumed parameters. Briefly, contaminants are searched for within 10 *TESS* pixels of the target, and the contaminating flux is calculated within a radius that depends on the target's *TESS* magnitude and uses a PSF that is based on prelaunch PSF measurements of the field center (note that the PSF model does not attempt to account for bleed trails from very bright stars). The flux contamination reported is simply the ratio of the total contaminant flux to the target star flux (Figure 13). See Section 3.2.3 of Stassun et al. (2018) for more details.

3.2.2. Monte Carlo Determination of Parameter Uncertainties

We have implemented a Monte Carlo based approach to improve the final uncertainty estimates for the stellar parameters reported in the CTL, in which we perturb each observed quantity 1000 times and carry the perturbed values through the calculations to obtain a distribution for each derived quantity. We then report the 16th and 84th percentiles of those distributions as the corresponding lower and upper error bars. We have done this for two main reasons. First, we wish to be able to report asymmetric errors to better reflect the nature of the parameter posteriors. Second, a simple summation in quadrature of the underlying parameter errors overestimates the final uncertainty. This overestimation of the final uncertainty is particularly severe for the stellar radius because the distance error enters four times (D, G, $T_{\rm eff}$, BC_G), the errors from the reddening maps enter three times (G, $T_{\rm eff}$, BC_G), the error from the $T_{\rm eff}$ calibration enters twice ($T_{\rm eff}$, BC_G), and photometric errors in $G_{\rm BP} - G_{\rm RP}$ enter twice ($T_{\rm eff}$, BC_G).

In what follows, we represent Monte Carlo perturbed quantities with primed (or double-primed) symbols and nominal values with unprimed symbols. In addition, $\mathcal{N}$ represents a normal Gaussian deviate (mean = 0, $\sigma = 1$) that is used to perturb the nominal quantities. Once a quantity is perturbed, we use the same perturbed value throughout the procedure in order to preserve parameter correlations. For perturbing quantities with asymmetric error bars, we assume

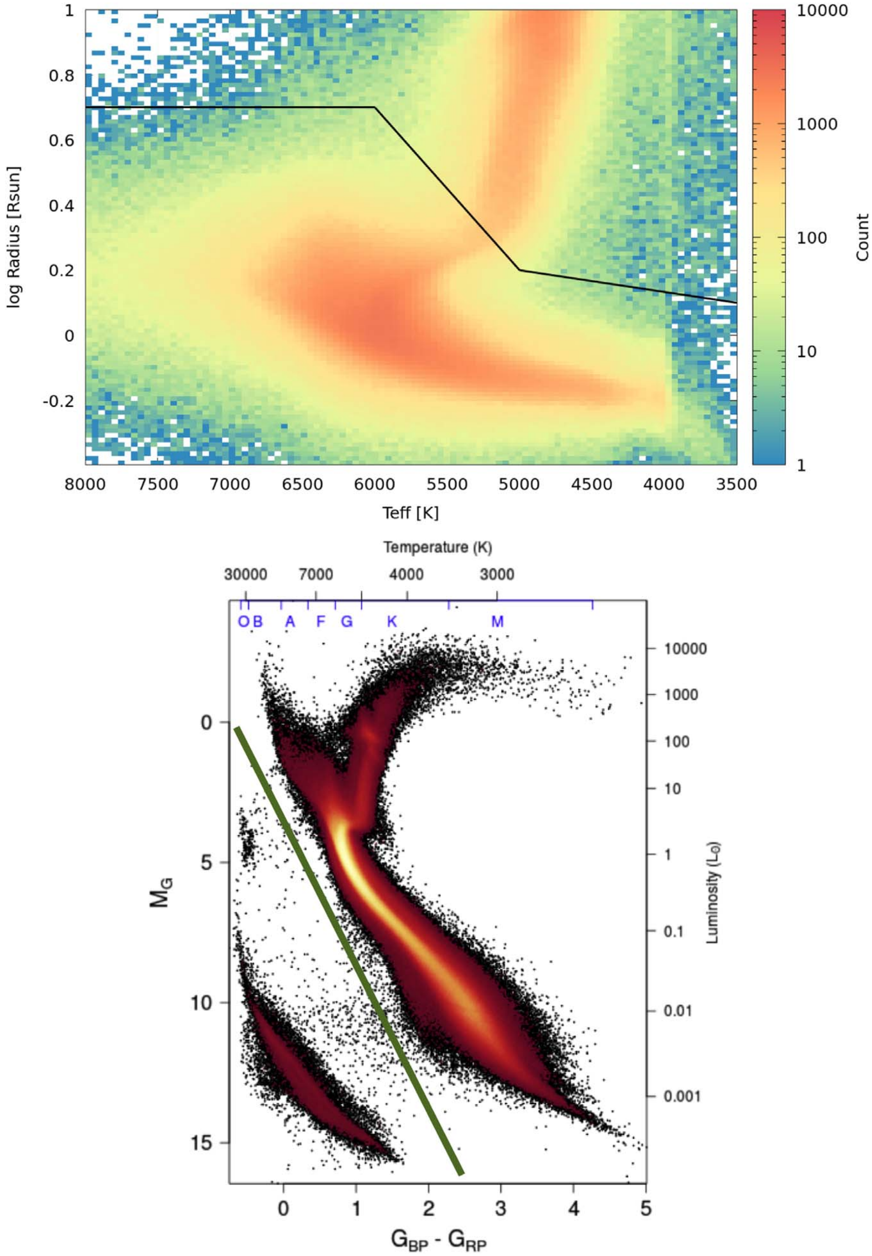

Figure 11. Top: radius versus $T_{\rm eff}$ for stars with calculated parameters in the TIC, showing the basis for the radius cuts adopted to include dwarfs and subgiants but exclude red giants from the calculation of mass and log g. Bottom: M_G versus $G_{\rm BP} - G_{\rm RP}$ diagram reproduced from Figure 2 of Gaia Collaboration et al. (2019), with a line drawn by eye showing the basis for the color–magnitude cut adopted to exclude white dwarfs from the calculation of mass and log g. The equation for this line is $M_G = 5.15\ (G_{\rm BP} - G_{\rm RP}) + 4.12$.

each side is reasonably well represented by a Gaussian distribution, and we use the lower error bar if the Gaussian deviate is negative or the upper error bar otherwise.

The procedure follows the steps below, in sequence:

1. Perturb the stellar distance: $D' = D + \mathcal{N} \times \{\sigma_{D,\rm low}, \sigma_{D,\rm high}\}$.
2. Perturb the reddening, which involves two contributions: one from the distance, and another from the intrinsic dust map errors. Query the dust map(s) with D' to obtain a perturbed reddening $E(B-V)''$. For Pan-STARRS, find the 16th and 84th percentiles of the reddening distribution at the nominal distance, and subtract from reddening at nominal distance to obtain the intrinsic dust map errors, $\{\sigma_{\rm red,low}, \sigma_{\rm red,high}\}$. For Schlegel et al. (1998), adopt $\sigma_{\rm red,low} = \sigma_{\rm red,high} = 0.01$ mag, derived from typical Pan-STARRS errors for stars outside the Galactic plane.[35] Then compute $E(B-V)' = E(B-V)'' + \mathcal{N} \times \{\sigma_{\rm red,low}, \sigma_{\rm red,high}\}$, and calculate reddening and extinction in the *Gaia* passbands with $E(G_{\rm BP} - G_{\rm RP})' = 1.31 E(B-V)'$ and $A(G)' = 2.72 E(B-V)'$.
3. Perturb the *Gaia* color and magnitude using the photometric errors: $(G_{\rm BP} - G_{\rm RP})' = (G_{\rm BP} - G_{\rm RP}) + \mathcal{N} \times \sigma_{G_{\rm BP}} + \mathcal{N} \times \sigma_{G_{\rm RP}}$, and $G' = G + \mathcal{N} \times \sigma_G$.

[35] Note that this implies the final uncertainties from our Markov chain Monte Carlo (MCMC) estimates are likely to be underestimated for stars within the plane or south of −30° decl.

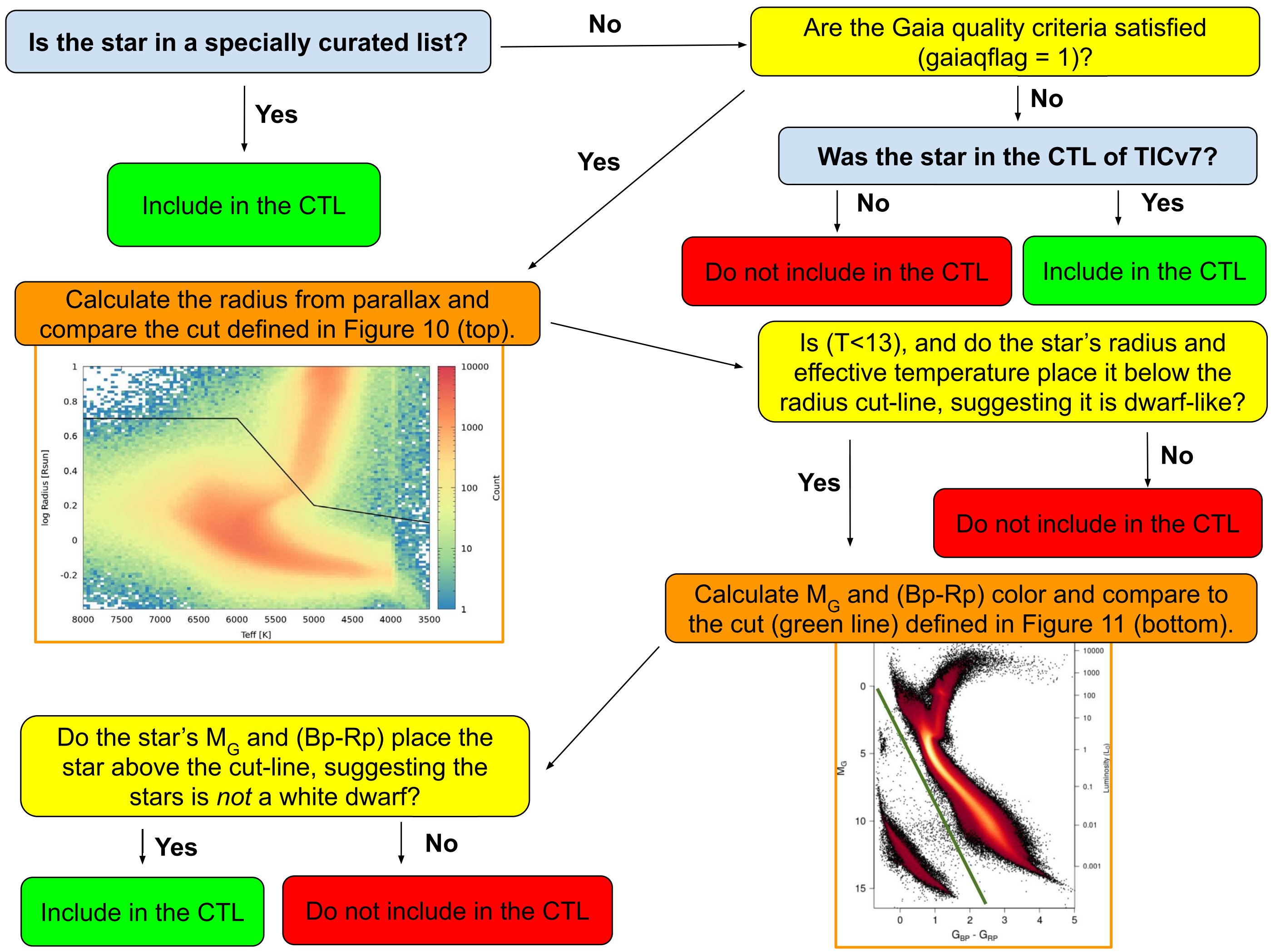

Figure 12. Visual schematic of the logic flow by which stars are selected from the TIC into the CTL.

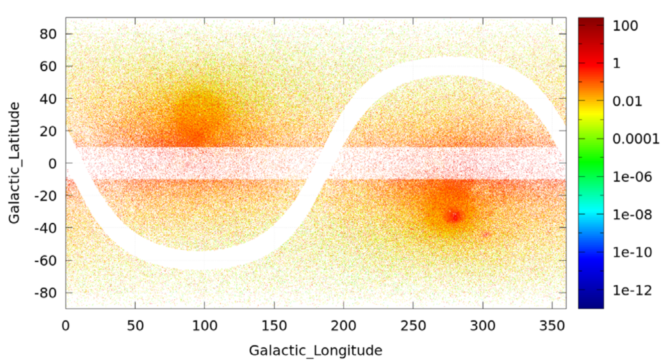

Figure 13. Flux contamination as a function of sky position in TICv8.

4. Deredden the perturbed *Gaia* color and magnitude: $(G_{\rm BP} - G_{\rm RP})'_{\rm dered} = (G_{\rm BP} - G_{\rm RP})' - E(G_{\rm BP} - G_{\rm RP})'$ and $G'_{\rm dered} = G' - A(G)'$.
5. Compute the perturbed and dereddened *TESS* magnitude $T'_{\rm dered}$ with the expression in Section 2.3.1 using $G'_{\rm dered}$ and $(G_{\rm BP} - G_{\rm RP})'_{\rm dered}$. Calculate the perturbed extinction in the T band as $A(T)' = 2.06E(B - V)'$. Then apply the extinction and compute the final perturbed apparent *TESS* magnitude (i.e., affected by extinction) as $T' = T'_{\rm dered} + A(T)' + \mathcal{N} \times \sigma_T$, where σ_T is the scatter of the T calibration.
6. Compute the perturbed $T_{\rm eff}$: $T'_{\rm eff} = T'_{\rm eff,dered} + \mathcal{N} \times \sigma_{T_{\rm eff}}$, where $T'_{\rm eff,dered}$ is the perturbed temperature derived from the perturbed dereddened color, and $\sigma_{T_{\rm eff}} = 122$ K (Section 2.3.4).
7. Compute the perturbed radius (R') from the perturbed bolometric correction (BC$'$), $T'_{\rm eff}$, D', and $G'_{\rm dered}$, where $\mathrm{BC}' = \mathrm{BC}(T'_{\rm eff}) + \mathcal{N} \times \sigma_{\rm BC}$, and $\sigma_{\rm BC}$ is a function of $T'_{\rm eff}$.
8. Compute the perturbed mass as $M' = M(T'_{\rm eff}) + \mathcal{N} \times \{\sigma_{M,\rm low}, \sigma_{M,\rm high}\}$, where σ_M is a function of $T'_{\rm eff}$. Then compute the perturbed $\log g$, luminosity, and mean density as $\log g' = 4.4383 + \log M' - 2 \log R'$, $L' = (R')^2 (T'_{\rm eff}/5772)^4$, and $\rho' = M'/(R')^3$.

3.3. Target Prioritization

Ultimately, one of the most fundamental characteristics reported in the CTL is the target priority, which allows the selection of the most suitable stellar candidates for 2 minute cadence. The target priority calculated in the CTL of TICv8 uses a schema identical to the priority calculation in the CTL of TICv7. For a more detailed derivation of the priority formula, we direct the reader to Stassun et al. (2018). However, we provide a basic explanation below.

The priority in TICv8 determines the relative ability of *TESS* to detect small planetary transits and is calculated using the radius of the star (R), the total expected photometric precision (σ), and a priority boost factor that scales with a probabilistic model of the expected number of sectors (N_S) any given star could fall in. Typically, the closer the star is to the ecliptic north or south pole, the larger the boost factor. This leads to the following formulation of stellar priority:

$$\frac{\sqrt{N_S}}{R^{1.5} \times \sigma}. \quad (10)$$

This priority is then normalized by the priority for a star with $R = 0.1 R_\odot$, $N_S = 12.654$ sectors, and $\sigma = 61.75$ ppm to force the priority to be on a scale from 0 to 1. Finally, there is a small subset of stars that are manually deprioritized based on known issues with current TIC calculations or known limitations of the *TESS* observing plan. These are as follows:

1. Stars close to the Galactic plane ($|b| < 10°$) are multiplied by a factor of 0.1 in order to deprioritize stars that may be affected by a poor understanding of their true reddening. Stars in the specially curated lists are excluded from this condition.
2. Stars with $\log g$ values greater than 5 have had their priorities set to 0 and their properties set to Null, to avoid biases from poor-quality effective temperature, extinction, or parallax measurements. Stars in the specially curated lists are excluded from this condition.
3. Stars close to the ecliptic plane ($|\beta| \lesssim 6°$) are not expected to be observed as part of the main mission, due to a gap in camera coverage between the Southern and Northern observations. Therefore, their N_S values are 0, and thus the priority is 0.

For the first year of the *TESS* prime mission observing the southern ecliptic sky (*TESS* Sectors 1–13), CTLv7 priorities were used to select targets. For the second year of the prime mission observing the north (Sectors 14–26), priorities from CTLv8 are being used. If the *TESS* mission is extended and if 2 minute cadence targets are selected for observation by the mission itself for transit detection, it will be possible to continue using CTLv8 priorities to select targets, though some alteration may be required if an extended mission observes targets in the (currently excluded) ecliptic plane.

3.4. Performance of the CTL in the First Year of TESS *Observations*

Because the estimated stellar radius is such an important factor in our target prioritization, we conclude by examining the extent to which the nominal dwarf targets in the first year of *TESS* observations (based on CTLv7) were in fact giants or subgiants. As discussed in Stassun et al. (2018), based on the method of reduced proper motion that we had employed, it was expected that the contamination of CTLv7 by giants would be only ~3% but that the contamination by subgiants would be ~40%. We examine those predictions by checking the evolutionary class of the set of *TESS* 2 minute cadence targets actually observed in Sectors 1–13.

In the first year of the mission, 247,899 objects were selected for 2 minute cadence observations in the northern ecliptic sky. Since a large number of these were observed in multiple sectors, the number that are unique is 128,292. Those objects were selected from several target lists, including the CTL itself but also lists from the asteroseismology program, the guest investigator program, and others. Here we examine targets of relevance to the mission's primary transit search, which were initially optimized to be dwarf stars, and which we here identify by CTLv7 priority of greater than 0.0011, that is, the priority cutoff that yields about 400,000 top-priority targets across the entire sky.

Since all stars in Sectors 1–13 brighter than $T = 6$ regardless of luminosity class were selected for observation regardless of priority (via the specially curated Bright Star list), here we examine the 122,669 unique stars with $T > 6$, of which 80,670 were among the top-priority targets in CTLv7 as defined above. Of those, 72,030 have reliable *Gaia* DR2 observations in TICv8 (i.e., `gaiaqflag` is set to 1), allowing us to reliably classify them as dwarfs, subgiants, or giants. We find that 81.8% are dwarfs, 15.7% are subgiants, and 2.5% are giants. These contamination rates are consistent with the predictions from Stassun et al. (2018) for the giants, but represents a lower contamination rate than predicted for the subgiants.

The reason for the smaller than expected fraction of subgiants is likely that the highest priority targets tend to be cool stars, for which the disambiguation of dwarfs from other luminosity classes is most secure (essentially because cool subgiants do not exist). In any case, a lower subgiant contamination is certainly beneficial for the ultimate mission goal of transit detection of small planets. As discussed in Section 2.3.5, we do not intentionally exclude subgiants from the updated CTL, although their priorities are again set relatively lower than dwarfs according to their larger radii via Equation (10).

4. Summary of Representative Properties of Stars in the TIC

Compared to TICv7, the number of stars in TICv8 has increased by a factor of ~3.5. The number of stars with $T_{\rm eff}$ has doubled, and the number with estimated radii has increased by a factor of ~20. Table 4 summarizes the numbers of stars in the TICv8 and CTLv8 for various representative subsets.

Figure 14 shows the overall distribution of *TESS* magnitudes (left) and $T_{\rm eff}$ (right). Note that our relations for estimating $T_{\rm eff}$ end at 15,000 K; hotter stars in the distribution originate from the specially curated list for hot subdwarfs. Figure 15 shows the overall distribution of radii for stars smaller than $10\,R_\odot$ (left) and log g (right). Stars with $R \geqslant 5\,R_\odot$ are regarded as giants, and we do not report masses or other derived properties for them. Our relations for masses are designed principally for dwarfs and work reliably well also for subgiants, but are not reliable for giants.

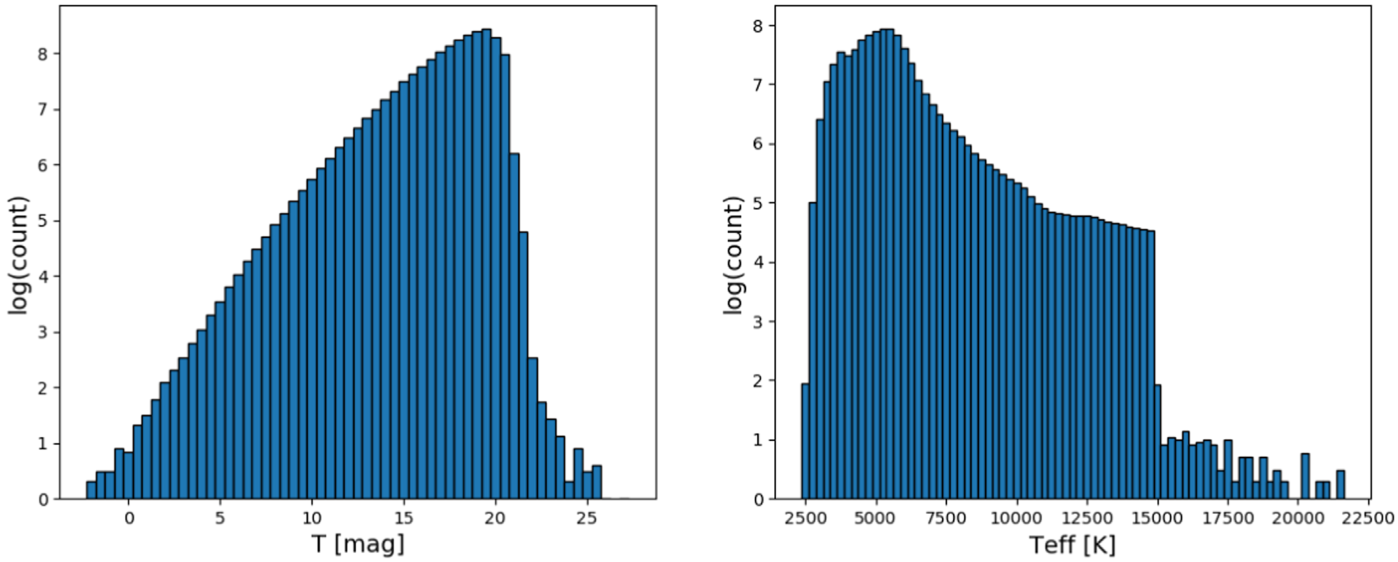

Figure 14. TICv8 distributions of T (left) and T_{eff} (right).

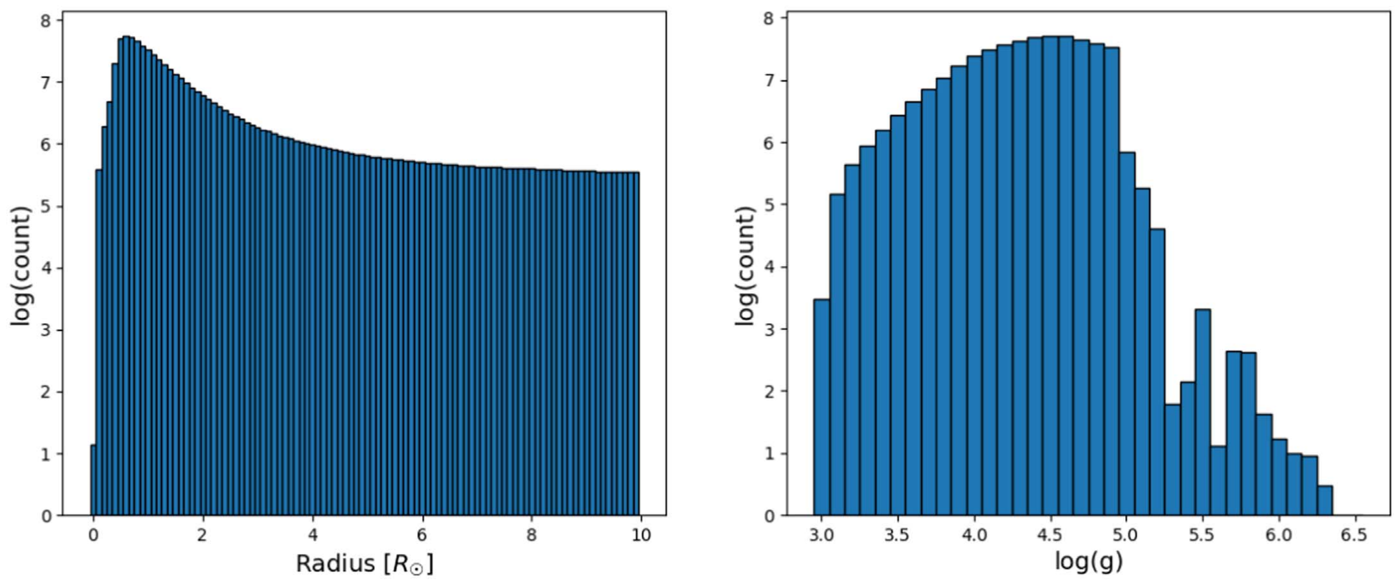

Figure 15. TICv8 distributions of stellar radius for stars smaller than 10 $R_\odot$ (left) and log g (right).

Table 4
Summary of Basic Stellar Properties in the TIC and CTL

Quantity	Number of Stars		Subpopulation	Number of Stars		
	TICv7	TICv8		TICv7	TICv8	CTLv8
T magnitude	470,995,593	1,726,340,024	$T < 10$	966,297	912,552	268,752
T_{eff}	331,414,942	683,248,319	$T_{\text{eff}} < 4500$ K	991,868	140,614,051	4,053,071
Radius	27,302,067	541,007,000	$R < 0.5\ R_\odot$	787,924	27,804,756	1,568,574
Mass	27,302,066	455,211,680	$M < 0.5\ M_\odot$	741,483	14,113,970	1,587,663
Spectroscopic T_{eff}	572,363	4,059,381	Spect. $T_{\text{eff}} < 6000$ and log $g > 4.1$	395,144	1,673,350	420,443
Proper motion	316,583,013	1,335,789,302	Proper motion >1000 mas yr^{-1}	655	1092	498
Parallax	2,045,947	1,269,096,797	Distance < 100 pc	42,454	574,927	217,245

Note. Note that the TICv7 subpopulations for cool T_{eff}, small radii, and low mass reflect numbers from CTLv7, because in TICv7 these quantities were computed only for stars in the CTL.

We gratefully acknowledge partial support for this effort from NASA grant 17-XRP17 2-0024. Funding for the *TESS* mission is provided by NASA's Science Mission directorate. P.S.M. acknowledges support from the NASA Exoplanet Research Program (XRP) under grant No. NNX15AG08G issued through the Science Mission Directorate. B.R.-A. acknowledges funding support from CONICYT PAI/CONCURSO NACIONAL INSERCIÓN EN LA ACADEMIA, CONVOCATORIA 2015 79150050 and FONDECYT through grant 11181295. This work is partly supported by JSPS KAKENHI grant Nos. JP18H01265 and JP18H05439, and JST PRESTO grant No. JPMJPR1775. This work has made extensive use of the Filtergraph data visualization service (Burger et al. 2013). This work has made use of data from the European Space Agency (ESA) mission *Gaia* (https://www.cosmos.esa.int/gaia), processed by the *Gaia* Data Processing and Analysis Consortium (DPAC, https://www.cosmos.esa.int/web/gaia/dpac/consortium). Funding for the DPAC has been provided by national institutions, in particular the institutions participating in the *Gaia* Multilateral Agreement. This work has also made use of the SIMBAD database and the VizieR catalog access tool, both operated at the CDS, Strasbourg, France, and of NASA's Astrophysics Data System Abstract Service. The remarkably careful review of the original manuscript by the anonymous referee is very gratefully acknowledged.

Appendix A
Specially Curated Lists

The specially curated lists from TICv7 (Stassun et al. 2018) have been updated as follows.

A.1. Cool Dwarf List

The Cool Dwarf list has been updated. It is incorporated into the TIC and CTL as a total override, meaning that values in this list supersede and replace default values calculated by the usual TIC/CTL procedures. J. Chittidi et al. (2019, in preparation) provides detailed procedures. Here we briefly summarize the main changes compared to the Cool Dwarf list that was incorporated into the previous version of the TIC/CTL (Muirhead et al. 2018; Stassun et al. 2018).

For TICv8, the Cool Dwarf specially curated list was revised and substantially augmented to include newly available astrometric parallax measurements and photometry from the *Gaia* mission. The First Cool Dwarf Catalog (CDC1) used primarily reduced proper-motion measurements to identify nearby cool dwarfs. This led to deficiencies in the southern hemisphere from a lack of long time-baseline all-sky surveys (see Muirhead et al. 2018 for a detailed description). The incorporation of *Gaia* DR2 parallaxes resolved this incompleteness. The Second Cool Dwarf Catalog (CDC2) was built from the "nearest neighbor" cross-match between *Gaia* DR2 sources and the Two Micron All Sky Survey Point Source Catalog (2MASS PSC; Cutri et al. 2013), available on the *Gaia* Archive. The cross-matched catalog was queried for all objects with the following criteria:

1. Nonzero astrometric parallax measurement with a signal-to-noise ratio of at least 5.
2. A single and unique entry in the 2MASS PSC, and a photometric quality flag of "C" or better for all 2MASS magnitudes.
3. Absolute K_S-band magnitude (M_K) between 4.5 and 10.0.
4. $V - J$ color greater than 2.7, to identify cool stars and maintain consistency with CDC1.
5. Absolute V-band magnitude (M_V) that meets the following criterion: $M_V > 2.2\ (V - J) - 2$.
6. *Gaia* $G_{\rm RP}$-band magnitude less than 18.

For the absolute magnitude calculations, distances were taken from Bailer-Jones et al. (2018). The V-band magnitude was calculated using $G_{\rm BP}$ and $G_{\rm RP}$ magnitudes and the conversion published by Jao et al. (2018). No extinction or reddening corrections were applied in the query. Furthermore, any objects that did not meet these criteria, but were in the CDC1 with parameters determined from non-*Gaia*-based parallaxes, were manually added to the CDC2. For example, nearby M dwarfs with saturated 2MASS magnitudes were kept in the CDC2 using parameters from the CDC1.

The result from the query was cross-matched with the original Cool Dwarf Catalog (Muirhead et al. 2018), including all entries from both catalogs. For each entry, we calculated stellar mass, stellar radius, effective temperature, and *TESS* magnitude, assuming each entry is a single star and ignoring effects from reddening and extinction.

Stellar masses and radii were calculated using the mass–M_K relations from Mann et al. (2019) and the radius–M_K relations from Mann et al. (2015), both valid for $4.5 < M_K < 10.0$. Objects outside of this range or lacking an astrometric parallax were flagged for removal. Effective temperature and T were calculated from $G_{\rm BP}$ and $G_{\rm RP}$ magnitudes using custom relations developed from photometrically calibrated spectra from Mann et al. (2013). Objects in the CDC1 without unique 2MASS identifiers were flagged for removal.

Figure 16 shows histograms and cumulative distribution functions comparing CDC1 and CDC2 for T and $T_{\rm eff}$. CDC2 removed a handful of bright and low-temperature CDC1 entries owing to the parallax and M_K criteria. For example, the brightest object in the CDC1 is α Centauri B, a K1 dwarf that does not meet the new M_K criteria. For context, Figure 17 compares the spatial distribution of CDC stars in CDC2 versus CDC1, showing especially the substantially improved coverage of the southern sky (including especially the southern CVZ) in CDC2.

Due to the CDC's use of specialized relations for determining T, we observe an offset of $\sim$0.1 mag between T as computed in the CDC versus T computed by our nominal relations (see Section 2.3.1). The difference can be as large as $\sim$1 mag at the faintest end of the TIC ($T \gtrsim 18$). Because we adopt the CDC values as an override, these offsets will only be noticeable when comparing similar stars where one is in the CDC and the other is not.

Finally, the $T_{\rm eff}$ values computed in the CDC versus the standard TIC relations are in good agreement, especially for TIC $T_{\rm eff}$ derived from *Gaia* colors; the scatter is even lower than the 122 K that we assume for the standard TIC $T_{\rm eff}$. However, stars with $T_{\rm eff}$ inherited from TICv7 can differ more substantially, especially stars with high $T_{\rm eff}$ derived using a photometric B magnitude (provenance flag "bphotvk"); these should be checked independently before being used.

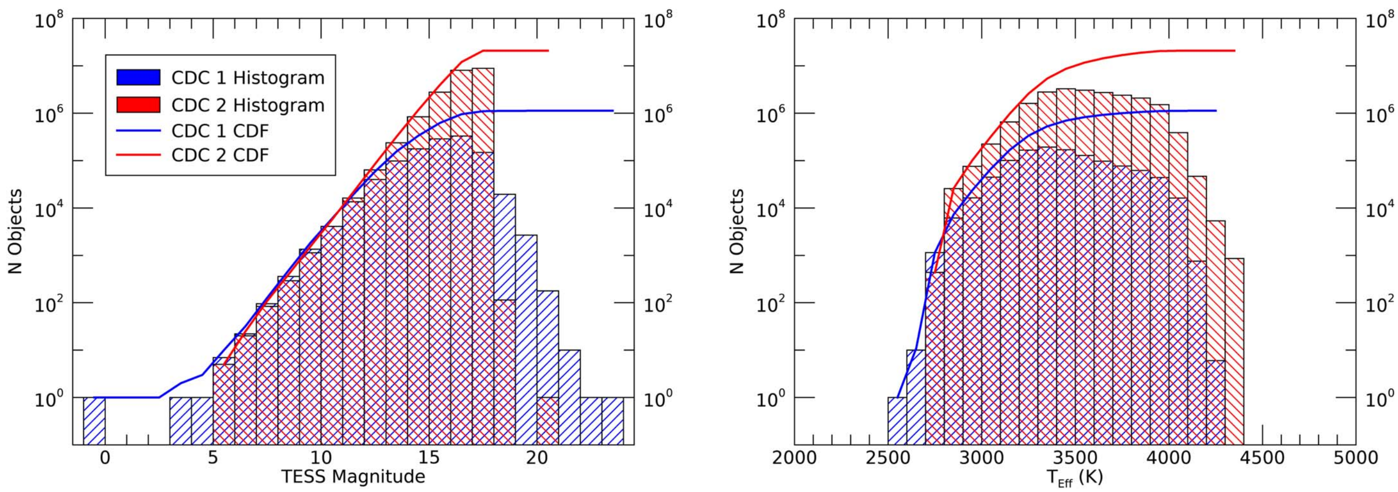

Figure 16. Histograms and cumulative distribution functions comparing the updated Cool Dwarf Catalog (CDC2) to that which was incorporated into the previous TIC/CTL (CDC1), for T (left) and $T_{\rm eff}$ (right). Several bright objects in CDC1 were excluded from CDC2 owing to the requirements on M_K. Additionally, the requirement that $G_{\rm RP} < 18$ reduces the number of faint cool dwarfs with T greater than 18. CDC2 lacks objects with $T_{\rm eff}$ less than 2700 K.

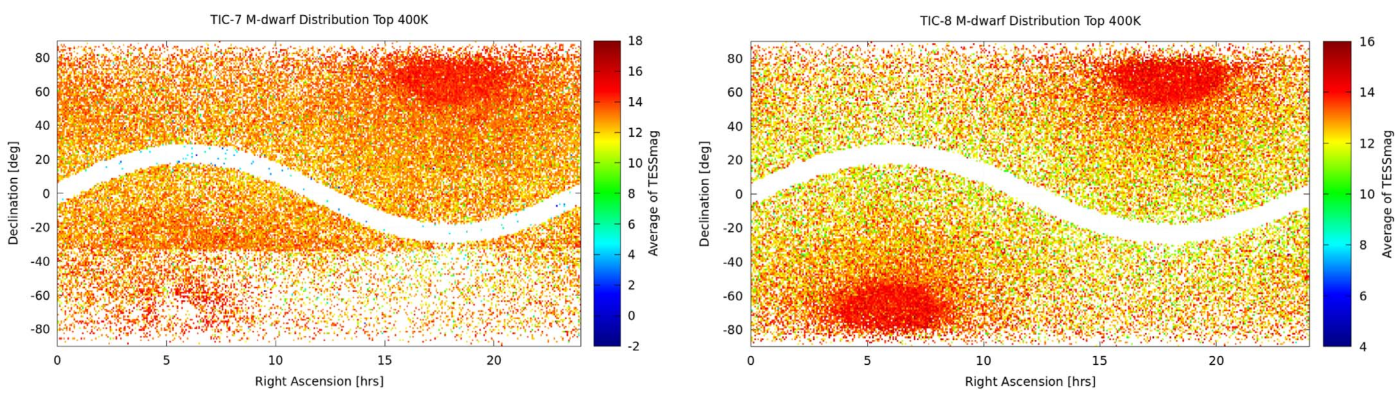

Figure 17. Comparison of the distribution of identified cool dwarfs in TICv7 (left) and TICv8 (right) in the top 400 K targets.

A.2. Known Planet Hosts

About 3000 stars are known to host exoplanets, of which ∼2800 are systems for which the radial velocity and transit methods were used for discovery. There are a variety of scientific reasons why *TESS* observations of these stars would be valuable, such as detecting stellar variability (Dragomir et al. 2012), transit ephemeris refinement for follow-up observations (Kane et al. 2009), detecting transit timing variations (TTVs) to help identify additional planets or stellar companions, potential discovery of further transiting planets in those systems, and so on. We worked to include all known planet hosts in previous versions of the TIC, and these stars were also selected in a Cycle 1 *TESS* Guest Investigator program, ensuring that they are observed at 2 minute cadence.

While we have continued to make sure that all known planet hosts are included in the updated TIC, the stellar parameters of those stars were determined according to the standard procedures outlined in this paper. Those procedures, as noted, are based on large catalogs and do not take advantage of the precise measurements of individual systems that are typically conducted when the planets are discovered. We explored the option to adopt a curated set of the stellar parameters of the planet hosts to improve those quantities in the TIC by incorporating the exoplanet host star parameters listed in the NASA Exoplanet Archive (Akeson et al. 2013). Unfortunately, that catalog, along with all other catalogs of exoplanet host parameters that we explored, are by nature somewhat incomplete and heterogeneous. We have been unable as yet to adopt the set of host star parameters from such a catalog without requiring star-by-star customization of the stellar property fields to maintain the levels of internal consistency that the TIC itself adheres to. We therefore decided not to adopt this information for the current TIC.

We do not expect this change in the treatment of known exoplanet hosts to have major effects on the TIC. All such stars are still listed in the TIC, and we have no reason to believe that their stellar parameters—as determined through the procedures described in this paper along with all other TIC stars—are any less reliable than the rest of the TIC stars of similar stellar types. Known planet host stars can still be observed for various science goals by *TESS*, and the only impact that the absence of highly curated parameters will present is a less precise determination of resulting transit properties from the default *TESS* transit search pipeline. However, individual investigators can always recalculate such properties themselves using published stellar information.

A.3. Other Lists

1. *Bright Stars:* No longer exists; bright stars are included in the TIC but not as a specially curated list with separate procedures nor with special priorities.
2. *Hot Subdwarfs:* Has been updated; these are incorporated into the TIC and CTL as a total override.
3. *Guest Investigator Targets:* We import proposed GI Cycle 2 targets that did not have a preexisting TIC ID as new objects.

Appendix B
Provenance Flags in the TIC

B.1. Provenance Flags in Earlier Versions of the TIC

Table 5 presents a summary of data provenance flags used in TICv8 and in previous TIC versions.

B.2. Provenance Flags New to TICv8

Table 6 presents a summary of data provenance flags newly introduced in TICv8.

Table 5
Brief Description of Flags in TICv8 and Earlier TIC Versions

Column	Name	Flags	Description
12	Objtype	⋯	Flag to identify the object's type
⋯	⋯	star	object is a star
⋯	⋯	extended	object is a galaxy/extended source
13	Typesrc	⋯	Flag to identify the source of the object
⋯	⋯	gaia2	stellar source from *Gaia* DR2
⋯	⋯	hip	stellar source is *Hipparcos*
⋯	⋯	cooldwarfs or cdwrf	stellar source is the Cool Dwarf list
⋯	⋯	2mass	stellar source is 2MASS
⋯	⋯	lepine	stellar source is Lepines All-sky Catalog of Bright M Dwarfs (2011)
⋯	⋯	tmgaia	stellar source from *Gaia* with unique 2MASS match
⋯	⋯	tmmgaia	stellar source from *Gaia* without unique 2MASS match
⋯	⋯	hotsd or hotsubdwarf	stellar source is the Hot Subdwarf list
⋯	⋯	gicycle1	stellar source is the GI cycle 1 program
⋯	⋯	astroseis	stellar source from the T asteroseismology task group
16	Posflag	⋯	Flag to identify the source of the object's position
⋯	⋯	gaia2	stellar source from *Gaia* DR2
⋯	⋯	hip	stellar source is *Hipparcos*
⋯	⋯	cooldwarfs or cdwrf	stellar source is the Cool Dwarf list
⋯	⋯	2mass	stellar source is 2MASS
⋯	⋯	lepine	stellar source is Lepine All-sky Catalog of Bright M Dwarfs (2011)
⋯	⋯	tmgaia	stellar source from *Gaia* with unique 2MASS match
⋯	⋯	tmmgaia	stellar source from *Gaia* without unique 2MASS match
⋯	⋯	hotsd or hotsubdwarf	stellar source is the Hot Subdwarf list
⋯	⋯	gicycle1	stellar source is the GI cycle 1 program
⋯	⋯	2MASSEXT	extended source from 2MASS extended source catalog
⋯	⋯	astroseis	stellar source from the T asteroseismology task group
21	PMFlag	⋯	Flag to identify the source of the object's proper motion
⋯	⋯	gaia2	proper motions from *Gaia* DR2
⋯	⋯	ucac4	proper motions from UCAC4
⋯	⋯	tgas	proper motions from Tycho2-*Gaia* Astrometric Solution
⋯	⋯	sblink	proper motions from SuperBlink
⋯	⋯	tycho2	proper motions from Tycho2
⋯	⋯	hip	proper motions from *Hipparcos*
⋯	⋯	ucac5	proper motions from UCAC5
⋯	⋯	hsoy	proper motions from Hot Stuff for One Year
24	PARFlag	⋯	Flag to identify the source of the object's parallax
⋯	⋯	gaia2	parallax from *Gaia* DR2
⋯	⋯	tgas	parallax from Tycho2-*Gaia* Astrometric Solution
⋯	⋯	hip	parallax from *Hipparcos*
63	TESSFlag	⋯	Flag to identify the source of the object's T magnitude
⋯	⋯	goffs	magnitude calculated from offset with *Gaia* magnitude
⋯	⋯	gpbr	magnitude calculated from *Gaia* DR1 G mag and 2MASS photographic B mag
⋯	⋯	gbprp	magnitude calculated from *Gaia* $G_{\mathrm{BP}} - G_{\mathrm{RP}}$ color
⋯	⋯	rered	magnitude calculated from de-reddened *Gaia* colors, then re-reddened
⋯	⋯	hotsd or hotsubdwarf	magnitude adopted from Hot Subdwarf list
⋯	⋯	cooldwarfs or cdwrf	magnitude from Cool Dwarf list (Muirhead et al. 2018)
⋯	⋯	gaiak	magnitude calculated from G and 2MASS K_S
⋯	⋯	gaiaj	magnitude calculated from G and 2MASS J
⋯	⋯	joffset2	magnitude calculated from 2MASS J and an offset (+1.75 for $J - K_S > 1$)

Table 5
(Continued)

Column	Name	Flags	Description
⋯	⋯	hipvmag	magnitude calculated *Hipparcos* V magnitude
⋯	⋯	gaiaoffset	magnitude calculated from G and an offset
⋯	⋯	hoffset	magnitude calculated from 2MASS H offset
⋯	⋯	vjh	magnitude calculated from V and 2MASS $J - H$
⋯	⋯	jhk	magnitude calculated from 2MASS $J - K_S$
⋯	⋯	vjk	magnitude calculated from V and 2MASS $J - K_S$
⋯	⋯	hotsd or hotsubdwarf	magnitude adopted from hot subdwarf list
⋯	⋯	vk	magnitude calculated from V and 2MASS K_S
⋯	⋯	joffset	magnitude calculated from 2MASS J offset (+0.5 for $J - K_S < -0.1$)
⋯	⋯	gaiav	magnitude calculated from G and V
⋯	⋯	tmvk	magnitude calculated from V and 2MASS K_S (same as vk)
⋯	⋯	from_apass_i	magnitude from Cool Dwarf list (Muirhead et al. 2018)
⋯	⋯	from_sdss_ik	magnitude from Cool Dwarf list (Muirhead et al. 2018)
⋯	⋯	gaiah	magnitude calculated from *Gaia* and 2MASS H
⋯	⋯	jh	magnitude calculated from 2MASS $J - H$
⋯	⋯	cdwarf	magnitude from Cool Dwarf list (Muirhead et al. 2018)
⋯	⋯	bpjk	magnitude calculated from photographic B and 2MASS $J - K_S$
⋯	⋯	voffset	magnitude calculated from V and offset
⋯	⋯	koffset	magnitude calculated from 2MASS K_S and offset
⋯	⋯	wmean_vk_jhk	magnitude from Cool Dwarf list (Muirhead et al. 2018)
⋯	⋯	lepine	magnitude from Lepine catalog
⋯	⋯	gicycle1	magnitude from GI Cycle 1 proposal
⋯	⋯	from_sdss_i	magnitude from Cool Dwarf list (Muirhead et al. 2018)
64	SPFlag	⋯	Flag to identify the source of the object's stellar characteristics
⋯	⋯	cooldwarfs or cdwrf	mass and radius from Cool Dwarf list (see Section A and Muirhead et al. 2018)
⋯	⋯	hotsd or hotsubdwarf	mass and radius from the Hot Subdwarf list (see Section A)
⋯	⋯	gaia2	characteristics computed from measured *Gaia*/DR2 parallax
⋯	⋯	spec7	characteristics computed using the spectroscopic Torres et al. (2010) relations
⋯	⋯	tic7	characteristics imported from TICv7
⋯	⋯	splin	characteristics imported from TICv7, spline relation

Table 6
Brief Description of New Provenance Flags in TICv8

Column	Name	Flags	Description
91	EBVFlag	⋯	Flag to identify the source of the object's reddening
⋯	⋯	0	The star is closer than 100 pc, no extinction applied
⋯	⋯	1	The reddening from Schlegel et al. (1998) is applied
⋯	⋯	2	The reddening from Green et al. (2018) is applied
107	TeffFlag	⋯	Flag to identify the source of the object's effective temperature
⋯	⋯	cooldwarfs or cdwrf	$T_{\rm eff}$ from the Cool Dwarf list
⋯	⋯	hotsd or hotsubdwarf	$T_{\rm eff}$ from the Hot Subdwarf list
⋯	⋯	spect	$T_{\rm eff}$ from spectroscopic catalogs
⋯	⋯	gaia2	$T_{\rm eff}$ from *Gaia* $G_{\rm BP} - G_{\rm RP}$ color
⋯	⋯	spec	$T_{\rm eff}$ imported from TICv7
112	gaiaqflag	⋯	Flag to identify the quality of the *Gaia* astrometric and photometric information
⋯	⋯	−1	insufficient information
⋯	⋯	0	poor-quality *Gaia* information
⋯	⋯	1	good-quality *Gaia* information
114	Vmagflag	⋯	Flag to identify the source of the object's V magnitude
⋯	⋯	gaia2	V magnitude calculated from *Gaia* $G_{\rm BP} - G_{\rm RP}$ color
⋯	⋯	ucac4	V magnitude calculated from ucac4 magnitude (see Stassun et al. 2018)
⋯	⋯	tycho2v3	V magnitude calculated from Tycho-V_T magnitude (see Stassun et al. 2018)
⋯	⋯	tycho2v	V magnitude calculated from Tycho-V_T magnitude (see Stassun et al. 2018)
⋯	⋯	tycho	V magnitude calculated from Tycho-V_T magnitude (see Stassun et al. 2018)
⋯	⋯	apassdr9	V magnitude imported from APASS DR9 (see Stassun et al. 2018)
⋯	⋯	apass	V magnitude imported from APASS DR7 (see Stassun et al. 2018)
⋯	⋯	sblink	V magnitude imported from SuperBlink (see Stassun et al. 2018)
⋯	⋯	mermil	V magnitude imported from the Mermilloid catalog (see Stassun et al. 2018)
⋯	⋯	cdwarf	V magnitude imported from the Cool Dwarf list (TICv6; see Stassun et al. 2018)
⋯	⋯	cdwrf	V magnitude imported from the Cool Dwarf list (TICv7; see Stassun et al. 2018)

Table 6
(Continued)

Column	Name	Flags	Description
…	…	sirful	*V* magnitude imported from the Sirful catalog (see Stassun et al. 2018)
…	…	hipvmag	*V* magnitude calculated using *Hipparcos* V (see Stassun et al. 2018)
…	…	gaiak	*V* magnitude calculated from *Gaia* DR1 *G* and 2MASS K_S (see Stassun et al. 2018)
115	Bmagflag	…	Flag to identify the source of the object's *B* magnitude
…	…	tycho2b3	*B* magnitude calculated from Tycho-B_T magnitude (see Stassun et al. 2018)
…	…	tycho2b	*B* magnitude calculated from Tycho-B_T magnitude (see Stassun et al. 2018)
…	…	tycho	*B* magnitude calculated from Tycho-B_T magnitude (see Stassun et al. 2018)
…	…	apassdr9	*B* magnitude imported from APASS DR9 (see Stassun et al. 2018)
…	…	bpbj	*B* magnitude calculated from 2MASS photometric *B* (see Stassun et al. 2018)
…	…	mermil	*B* magnitude imported from the Mermilloid catalog (see Stassun et al. 2018)
116	splists	…	Flag to identify if the object is in a specially curated list
…	…	cooldwarfs_v8	star is identified in the Cool Dwarf specially curated list
…	…	hotsubdwarfs_v8	star is identified in the Hot Subdwarf specially curated list

Appendix C
CTL Filtergraph Portal

Table 7 summarizes the contents of the enhanced CTL provided via the Filtergraph data visualization portal service at filtergraph.vanderbilt.edu/tess_ctl.

Table 7
Basic Description of All Quantities Found on the Filtergraph Portal

Descriptions of CTL Contents	
Column Name	Brief Description
Right_Ascension	Right ascension of the star, equinox J2000.0, epoch 2000.0 (degrees)
Declination	Declination of the star, equinox J2000.0, epoch 2000.0 (degrees)
Tess_mag	Calculated *TESS* magnitude
Teff	Adopted effective temperature (K)
Priority	Priority based on *T*, radius, and flux contamination with boosts and deboosts
Radius	Stellar radius derived from photometry ($R_\odot$)
Mass	Stellar mass derived from photometry ($M_\odot$)
ContamRatio	Ratio of contaminating flux to flux from the star
Observed	0 or 1 if the star has been observed already in 2 minute cadence
Sector	Sector (or combination of sectors) in which the star was observed
Galactic_Long	Longitude in the Galactic coordinate frame (degrees)
Galactic_Lat	Latitude in the Galactic coordinate frame (degrees)
Ecliptic_Long	Longitude in the ecliptic coordinate frame (degrees)
Ecliptic_Lat	Latitude in the ecliptic coordinate frame (degrees)
Parallax	Parallax of the star provided by either TGAS/*Gaia* or *Hipparcos* (mas)
Distance	Distance of the star provided (pc)
Total_Proper_Motion	Total proper motion of the star (mas yr^{-1})
V_mag	Adopted *V* magnitude
J_mag	2MASS *J* magnitude
H_mag	2MASS *H* magnitude
K_S_mag	2MASS K_S magnitude
G_mag	*Gaia* magnitude
u_mag	SDSS *u* magnitude
g_mag	SDSS *g* magnitude
r_mag	SDSS *r* magnitude
i_mag	SDSS *i* magnitude
z_mag	SDSS *z* magnitude
W1_mag	ALLWISE *W1* magnitude
W2_mag	ALLWISE *W2* magnitude
W3_mag	ALLWISE *W3* magnitude
W4_mag	ALLWISE *W4* magnitude
G_BP	*Gaia* DR2 BP magnitude
G_RP	*Gaia* DR2 RP magnitude
Hipparcos_Number	*Hipparcos* ID
Tycho2_ID	*Tycho-2* ID
2MASS_ID	2MASS ID
TICID	ID for the star in the *TESS* Input Catalog
Special_Lists	Identifies whether a star is in a special list
Priority_TIC4	Priority based on the TIC-4 schema
Priority_TIC5	Priority based on the TIC-5 schema
Priority_TIC6	Priority based on the TIC-6 schema
Priority_Non_Contam	Priority without neighbor contamination
Priority_No_Boost	Priority without sector boosting
Teff_Src	Source of the effective temperature (see `Teff` column)
Teff_Err	Error in the effective temperature (K)
Teff_Err_Pos	Estimated positive error in the effective temperature from MC (K)
Teff_Err_Neg	Estimated negative error in the effective temperature from MC (K)
EBMV	Applied extinction
EBMV_Err	Error in extinction
EBMV_Src	Identifies source of adopted extinction
StarChar_Src	Identifies source of adopted stellar parameters
Radius_Err	Uncertainty in the radius (solar)
Radius_Err_Pos	Estimated positive error in the stellar radius from MC (solar)
Radius_Err_Neg	Estimated negative error in the stellar radius from MC (solar)
Mass_Err	Uncertainty in the mass (solar)
Logg	Surface gravity (cgs)
Logg_Err	Uncertainty in the surface gravity (cgs)
Rho	Density (solar)
Rho_Err	Uncertainty in the density (solar)
Lum	Luminosity (solar)

Table 7
(Continued)

Descriptions of CTL Contents	
Column Name	Brief Description
Metallicity	Stellar metallicity from spectra, if available (dex)
Metallicity_Err	Stellar metallicity error from spectra, if available (dex)
Noise_Star	Uncertainty from the star counts
Noise_Sky	Uncertainty from the sky counts
Noise_Contaminates	Uncertainty from the neighboring star counts
Noise_Readout	Uncertainty in the detector readout
Noise_Systematics	Uncertainty floor
Distance_Err	Uncertainty in the distance (pc)
Distance_Err_Pos	Estimated positive error in the distance from MC (pc)
Distance_Err_Neg	Estimated negative error in the distance from MC (pc)

ORCID iDs

Keivan G. Stassun https://orcid.org/0000-0002-3481-9052
Ryan J. Oelkers https://orcid.org/0000-0002-0582-1751
Martin Paegert https://orcid.org/0000-0001-8120-7457
Guillermo Torres https://orcid.org/0000-0002-5286-0251
Joshua Pepper https://orcid.org/0000-0002-3827-8417
Nathan De Lee https://orcid.org/0000-0002-3657-0705
David W. Latham https://orcid.org/0000-0001-9911-7388
Philip S. Muirhead https://orcid.org/0000-0002-0638-8822
Bárbara Rojas-Ayala https://orcid.org/0000-0002-0149-1302
Scott W. Fleming https://orcid.org/0000-0003-0556-027X
Stephen R. Kane https://orcid.org/0000-0002-7084-0529
Thomas Barclay https://orcid.org/0000-0001-7139-2724
Jacob L. Bean https://orcid.org/0000-0003-4733-6532
David Charbonneau https://orcid.org/0000-0002-9003-484X
Andrew W. Mann https://orcid.org/0000-0003-3654-1602
Brian McLean https://orcid.org/0000-0002-8058-643X
Susan Mullally https://orcid.org/0000-0001-7106-4683
Norio Narita https://orcid.org/0000-0001-8511-2981
Peter Plavchan https://orcid.org/0000-0002-8864-1667
Dimitar Sasselov https://orcid.org/0000-0001-7014-1771
S. Seager https://orcid.org/0000-0002-6892-6948
Sanjib Sharma https://orcid.org/0000-0002-0920-809X
Alessandro Sozzetti https://orcid.org/0000-0002-7504-365X
Dennis Stello https://orcid.org/0000-0002-4879-3519
Roland Vanderspek https://orcid.org/0000-0001-6763-6562
Joshua N. Winn https://orcid.org/0000-0002-4265-047X

References

Abolfathi, B., Aguado, D. S., Aguilar, G., et al. 2018, ApJS, 235, 42
Akeson, R. L., Chen, X., Ciardi, D., et al. 2013, PASP, 125, 989
Andrae, R., Fouesneau, M., Creevey, O., et al. 2018, A&A, 616, A8
Arce, H. G., & Goodman, A. A. 1999, ApJL, 512, L135
Arenou, F., Luri, X., Babusiaux, C., et al. 2018, A&A, 616, A17
Bailer-Jones, C. A. L., Rybizki, J., Fouesneau, M., et al. 2018, AJ, 156, 58
Berger, T. A., Huber, D., Gaidos, E., & van Saders, J. L. 2018, ApJ, 866, 99
Bonifacio, P., Monai, S., & Beers, T. C. 2000, AJ, 120, 2065
Brewer, J. M., Fischer, D. A., Valenti, J. A., & Piskunov, N. 2016, ApJS, 225, 32
Brown, T. M., Latham, D. W., Everett, M. E., & Esquerdo, G. A. 2011, AJ, 142, 112
Buder, S., Asplund, M., Duong, L., et al. 2018, MNRAS, 478, 4513
Burger, D., Stassun, K. G., Pepper, J., et al. 2013, A&C, 2, 40
Cambrésy, L., Jarrett, T. H., & Beichman, C. A. 2005, A&A, 435, 131
Cardelli, J. A., Clayton, G. C., & Mathis, J. S. 1989, ApJ, 345, 245
Casagrande, L., & VandenBerg, D. A. 2014, MNRAS, 444, 392
Cutri, R. M., Wright, E. L., & Conrow, T. 2013, Explanatory Supplement to the AllWISE Data Release Products, http://wise2.ipac.caltech.edu/docs/release/neowise/expsup/
Deacon, N. R., Henning, T., & Kossakowski, D. E. 2019, MNRAS, 486, 251
Dragomir, D., Kane, S. R., Henry, G. W., et al. 2012, ApJ, 754, 37
Evans, D. W., Riello, M., De Angeli, F., et al. 2018, A&A, 616, A4
Gaia Collaboration, Babusiaux, C., van Leeuwen, F., et al. 2018, A&A, 616, A10
Gaia Collaboration, Brown, A. G. A., Vallenari, A., et al. 2016, A&A, 595, A2
Gaia Collaboration, Eyer, L., Rimoldini, L., et al. 2019, A&A, 623, A110
Gilmore, G., Randich, S., Asplund, M., et al. 2012, Msngr, 147, 25
Green, G. M., Schlafly, E. F., Finkbeiner, D., et al. 2018, MNRAS, 478, 651
Holmberg, J., Nordström, B., & Andersen, J. 2009, A&A, 501, 941
Huber, D., Bryson, S. T., Haas, M. R., et al. 2016, ApJS, 224, 2
Huber, D., Zinn, J., Bojsen-Hansen, M., et al. 2017, ApJ, 844, 102
Husser, T.-O., Kamann, S., Dreizler, S., et al. 2016, A&A, 588, A148
Jao, W.-C., Henry, T. J., Gies, D. R., & Hambly, N. C. 2018, ApJL, 861, L11
Kane, S. R., Mahadevan, S., von Braun, K., Laughlin, G., & Ciardi, D. R. 2009, PASP, 121, 1386
Kunder, A., Kordopatis, G., Steinmetz, M., et al. 2017, AJ, 153, 75
Lindegren, L. 2018, Gaia Technical Note, GAIA-C3-TN-LU-LL-124-01, http://www.rssd.esa.int/doc_fetch.php?id=3757412
Luo, A.-L., Zhao, Y.-H., Zhao, G., et al. 2015, RAA, 15, 1095
Maíz Apellániz, J., & Weiler, M. 2018, A&A, 619, A180
Mann, A. W., Dupuy, T., Kraus, A. L., et al. 2019, ApJ, 871, 63
Mann, A. W., Feiden, G. A., Gaidos, E., Boyajian, T., & von Braun, K. 2015, ApJ, 804, 64
Mann, A. W., Gaidos, E., & Ansdell, M. 2013, ApJ, 779, 188
Muirhead, P. S., Dressing, C. D., Mann, A. W., et al. 2018, AJ, 155, 180
Ricker, G. R., Winn, J. N., Vanderspek, R., et al. 2015, JATIS, 1, 014003
Sanders, J. L., & Das, P. 2018, MNRAS, 481, 4093
Schlafly, E. F., & Finkbeiner, D. P. 2011, ApJ, 737, 103
Schlegel, D. J., Finkbeiner, D. P., & Davis, M. 1998, ApJ, 500, 525
Sharma, S., Bland-Hawthorn, J., Binney, J., et al. 2014, ApJ, 793, 51
Sharma, S., Stello, D., Buder, S., et al. 2018, MNRAS, 473, 2004
Soubiran, C., Le Campion, J.-F., Brouillet, N., & Chemin, L. 2016, A&A, 591, A118
Stassun, K. G., Oelkers, R. J., Pepper, J., et al. 2018, AJ, 156, 102
Torres, G., Andersen, J., & Giménez, A. 2010, A&ARv, 18, 67